PHYSICAL REVIEW B **92**, 024506 (2015)

Ab initio theory of superconductivity in a magnetic field. II. Numerical solution

A. Linscheid,* A. Sanna, and E. K. U. Gross
Max Planck Institute of Microstructure Physics, Weinberg 2, D-06120 Halle, Germany
(Received 29 January 2015; revised manuscript received 9 June 2015; published 8 July 2015)

We numerically investigate the spin density functional theory for superconductors (SpinSCDFT) and the approximated exchange-correlation functional, derived and presented in the preceding Paper I [A. Linscheid *et al.*, Phys. Rev. B **92**, 024505 (2015)]. As a test system, we employ a free-electron gas featuring an exchange splitting, a phononic pairing field, and a Coulomb repulsion. SpinSCDFT results are compared with Sarma, the Bardeen-Cooper-Schrieffer theory, and with an Eliashberg type of approach. We find that the spectrum of the superconducting Kohn-Sham SpinSCDFT system is not in agreement with the true quasiparticle structure. Therefore, starting from the Dyson equation, we derive a scheme that allows to compute the many-body excitations of the superconductor and represents the extension to superconductivity of the G_0W_0 method in band-structure theory. This superconducting G_0W_0 method vastly improves the predicted spectra.

DOI: 10.1103/PhysRevB.92.024506 PACS number(s): 74.25.Ha, 74.25.Dw, 74.45.+c, 74.20.Fg

I. INTRODUCTION

Interaction between the magnetic and superconducting (SC) order leads to complex and fascinating phenomena. Apart from the Meissner effect as the most apparent aspect of this interaction on macroscopic length scales, for singlet SC, the ferromagnetic parallel spin alignment competes with spin antiparallel Cooper pair formation. While for triplet SC, such as UGe_2 a ferromagnetic (F) order is possible even in a bulk geometry [1], F/SC interfaces or SC surfaces in an external magnetic field allow to study the microscopic competition of a large spin splitting also for singlet SC. This may lead to spatial inhomogeneities of the SC order parameter, such as the phase predicted by Fulde and Ferrell and Larkin and Ovchinnikov [2,3]. Furthermore, the spin valve behavior of complex F/SC structures [4–6] may provide opportunities for novel devices making use of the unique electronic configuration that appears due to the vicinity of these two competing phases (see Ref. [7] for a review).

These effects are addressed in the theoretical literature so far mostly within model or semiempirical calculations due to the lack of a complete and efficient *ab initio* theory. This leaves the prediction of essential material-dependent properties as critical temperature and excitation gap in the presence of a magnetic field out of reach. The spin density functional theory for SC (SpinSCDFT) approach presented by Ref. [8] (hereafter referred to as I) may fill this gap, as the theory has the computational convenience of a Kohn-Sham (KS) density functional framework and allows to calculate material-dependent SC parameters from the crystal structure. The SpinSCDFT is in principle exact, but relies on the approximation of the exchange-correlation (xc) potential. A first approach to derive such an xc potential relies, in turn, on the Sham-Schlüter equation [9] for a SC [10] and is presented in I.

In this work, we present numerical results for SpinSCDFT, aiming to achieve a deeper understanding of this theoretical framework and to characterize and validate the xc potential, as derived in I. In particular, we will investigate the properties of the KS pairing function, that is a key object in SCDFT [11,12]. The test system we adopt for this analysis is a spin-splitted free-electron gas with a phononic and Coulomb coupling. Details of the model will be presented in Sec. II. One advantage of this simplified model with a homogeneous exchange splitting is its similarity to the starting point of Refs. [13,14] for their discussion of the Eliashberg equations and BCS theory, respectively. As compared to Ref. [13], we use a different notation (compare Paper I) and take a more general route which reduces to the earlier results in the case that the magnetic field homogeneously splits the electronic states. We will compute the temperature versus exchange splitting diagram of the model using, apart from SpinSCDFT, the BCS theory and the Eliashberg equations. Then, in Sec. V we will compare our SpinSCDFT results with the BCS approach (reviewed in Sec. III) and with the reference Eliashberg method (Sec. IV).

The SpinSCDFT KS system proves to give qualitatively correct results for the J-T diagram. However, we find in Sec. V that it does not show a physical excitation spectrum. A similar problem is very well known in conventional DFT, and is usually called the band-gap problem. Since the excitation gap is a very important property of SC, it is important to devolve methods to compute it. Therefore, the last part of this work will be devoted to describe an extension of the G_0W_0 method to our SC system and show that it entirely solves the problem, similar to its normal-state counterpart [15].

II. A TEST SYSTEM

The model system which we will use to investigate the SpinSCDFT formalism is based on a noninteracting electron gas under the influence of a homogeneous magnetic field B_0. The energy of its electronic states $\varepsilon_{k\sigma}$, relative to the Fermi energy E_f ($k = \boldsymbol{k},n$ where here n is a band index and we use the notation $-k = -\boldsymbol{k},n$), reads as

$$\varepsilon_{k\sigma} = \tfrac{1}{2}\boldsymbol{k}^2 - E_f - \mathrm{sign}(\sigma)\mu_B B_0 . \tag{1}$$

The Fermi energy is defined by integrating the density of states (DOS) up to E_f to have N_e electrons in the system. We set the density to $N_e/\Omega_{uc} = 1\, a_0^{-3}$ (a_0 is the Bohr radius and Ω_{uc} the unit-cell volume) which leads to a relatively

*Corresponding author: alinsch@mpi-halle.mpg.de

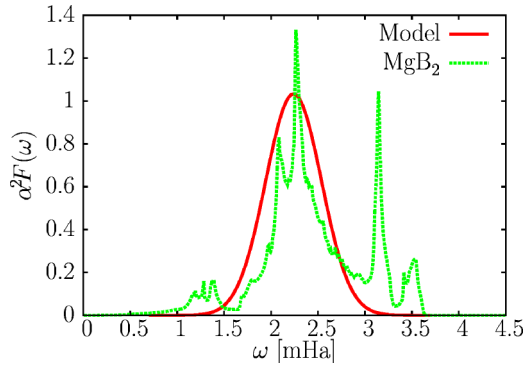

FIG. 1. (Color online) Model $\alpha^2F(\omega)$ function used in this work (full red line) as compared to that of MgB_2 (green dotted line).

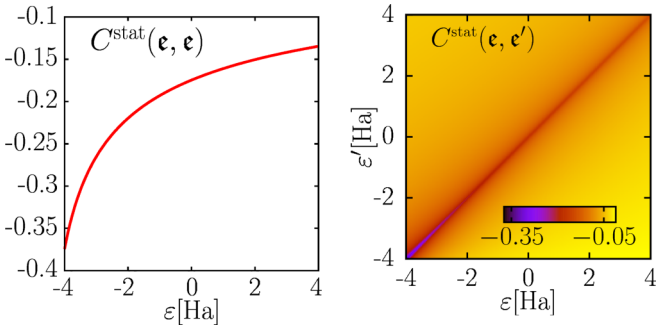

FIG. 2. (Color online) Screened Coulomb interaction function $C^{\rm stat}(\mathfrak{e},\mathfrak{e}')$ as given by the model expression in Eq. (3). The chosen model parameters are $E_f = 4.78$ Ha and $k_{\rm TF}^2 = (0.005)^2$ Ha.

large E_f of 4.78 Ha ignoring the small imbalance in up- and down-spin occupations. We also define a center of energy between spin-splitted states $\varepsilon(k) = \frac{1}{2}(\varepsilon_{k\uparrow} + \varepsilon_{-k\downarrow}) = \frac{1}{2}\boldsymbol{k}^2 - E_f$ and the splitting $J(k) = \frac{1}{2}(\varepsilon_{k\uparrow} - \varepsilon_{-k\downarrow}) = -\mu_{\rm B}B_0$. This will prove useful since, as seen in I, many SpinSCDFT entities depend on k only via these two parameters ε and J.

Superconductivity is induced in this model by an electron-phonon-like attractive interaction, expressed by the Gaussian Eliashberg function [16]

$$\alpha^2F(\omega) = \lambda\frac{\omega}{2}\frac{1}{\omega_w\sqrt{\pi}}e^{-\frac{1}{2}(\frac{\omega-\omega_0}{\omega_w})^2}. \tag{2}$$

This model depends on three parameters: λ, the electron-phonon coupling constant [16]; ω_0, the center of frequency of the optical branch of the phonon spectrum; and ω_w, the width of the optical branch. In the calculations we fix these numbers to $\omega_0 = 2.2$ mHa, $\omega_W = 0.5$ mHa, and $\lambda = 0.7$ which lead to coupling properties that are loosely similar to those of MgB_2 [17]. The resulting spectrum is plotted in Fig. 1 and compared with a calculated one of MgB_2. In SpinSCDFT one can consider a general Coulomb coupling on the same footing as the phonon interaction [11]. Here, we use a simple Thomas-Fermi–based model that was used before in SCDFT [11,18]. In this model, the screened Coulomb matrix element between a state of energy ε and one of energy ε' is given by

$$\begin{aligned} &C^{\rm stat}(\varepsilon,\varepsilon') \\ &\approx -\frac{\pi\rho^{\rm EG}(\varepsilon')}{2\sqrt{(\varepsilon+E_f)(\varepsilon'+E_f)}} \\ &\quad\times\ln\left(\frac{\varepsilon+\varepsilon'+2E_f+2\sqrt{(\varepsilon+E_f)(\varepsilon'+E_f)}+\frac{1}{2}k_{\rm TF}^2}{\varepsilon+\varepsilon'+2E_f-2\sqrt{(\varepsilon+E_f)(\varepsilon'+E_f)}+\frac{1}{2}k_{\rm TF}^2}\right). \end{aligned} \tag{3}$$

The screening parameter is chosen to be $k_{\rm TF}^2 = (0.005)^2$ Ha. With this parameter, the shape of the model $C^{\rm stat}(\varepsilon,\varepsilon')$ is shown in Fig. 2. All properties of the test system depend on the Bloch vector $\boldsymbol{k}$ and the band index n only via the single-particle energy ε_k. For brevity, we use the notation $\mathfrak{e} = (\varepsilon, J)$, $\int d\mathfrak{e} = \int d\varepsilon \int dJ$. Further, let $\delta(\mathfrak{e}-\mathfrak{e}') = \delta(\varepsilon-\varepsilon')\delta(J-J')$, then we may cast a Brillouin zone integral into the isotropic formulation with the double DOS:

$$\varrho(\mathfrak{e}) = \sum_k \delta\left(\varepsilon - \frac{\varepsilon_{k\uparrow}+\varepsilon_{-k\downarrow}}{2}\right)\delta\left(J - \frac{\varepsilon_{k\uparrow}-\varepsilon_{-k\downarrow}}{2}\right). \tag{4}$$

This quantity describes the number of states on equal center of energy ε and splitting J surfaces. In our model, the external field is homogeneous. This means the number of states on equal splitting surfaces has a delta distribution character that peaks at $J_0 = -\mu_{\rm B}B_0$. In the remainder of the paper, J_0 replaces the J integrals almost everywhere so we simplify the notation using $J_0 \to J$.

III. BCS THEORY WITH AN EXCHANGE SPLITTING

The J-T diagram of a BCS model with a homogeneous exchange splitting parameter J has been presented by Ref. [14]. This approach, that we are going to review here, can only be used to obtain qualitative results. Still, it will be an important guideline in understanding the more involved Eliashberg and SpinSCDFT results of the next sections. In a BCS model [19], one replaces the interactions among single electrons with an effective one, keeping only the matrix elements that couple the states $k,\uparrow$ and $-k,\downarrow$. The effective interaction is approximated with "a box" centered at the Fermi level (from $-\Omega_{\rm d}$ to $\Omega_{\rm d}$ which is of the order of the Debye phonon frequency to mimic phononic type of pairing and with height $-V$). This leads to a fixed-point equation for the mean-field gap Δ [14]:

$$\begin{aligned} \frac{1}{\rho(0)V} = \int_0^{\Omega_{\rm d}}\frac{d\varepsilon}{\sqrt{\varepsilon^2+\Delta^2}}&(f_\beta(J-\sqrt{\varepsilon^2+\Delta^2}) \\ &- f_\beta(J+\sqrt{\varepsilon^2+\Delta^2})). \end{aligned} \tag{5}$$

$\rho(0)$ is the DOS at the Fermi level and J is the splitting energy between up and down states. Apart from the solutions Δ of Eq. (5), there is also the trivial solution $\Delta = 0$. We solve Eq. (5) numerically as a function of T and J.[1] The solutions $\Delta(T,J)$ are presented in Fig. 3(a). There, we normalize Δ to Δ_0, the solution for $T \to 0$ and $J = 0$. Similarly, we normalize the J to Δ_0 and T to T_{c0}, the critical temperature for $J = 0$. In this way, we remove the explicit dependence on the parameters $\rho(0)V$ and $\Omega_{\rm d}$.

[1] We use $\Omega_{\rm d} = 0.2$ and $\rho(0)V = 1.0$ in the numerical calculation.

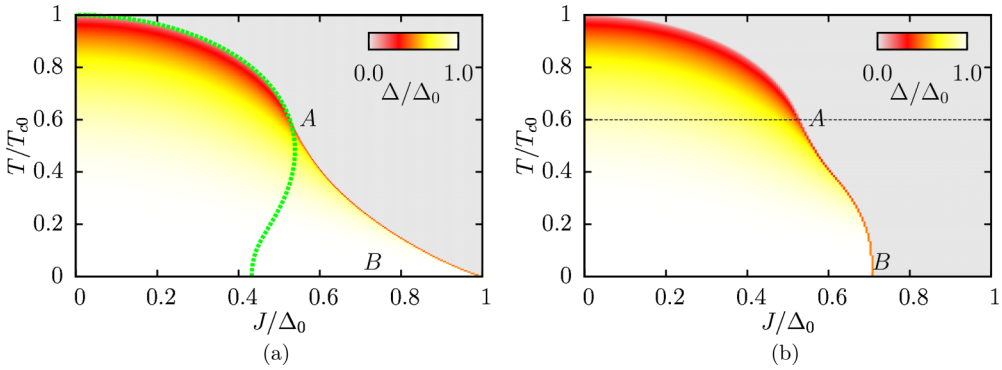

FIG. 3. (Color online) BCS solutions for a spin-splitted band structure [14]. In the panel (a) we plot the solution Δ if we can find one, while in (b) Δ is set to zero if the free energy favors the magnetic state. The green curve in (a) shows the $T_c(J)$ behavior from the linearized equation which has a curious shape that bends inwards. Below the thin dashed line in (b) at the label A at $T/T_{c0} \approx 0.6$ no solution with small Δ exists and the transition is of first order. Label B at $1/\sqrt{2}$ represents the Chandrasekhar-Clongston [20,21] limit.

When one attempts to linearize Eq. (5), a peculiar behavior is found in that the $T_c(J)$ curve bends inwards [14]. We solve a linearization of Eq. (5) and show the resulting $T_c(J)$ as a green line in Fig. 3(a). As pointed out by Refs. [14,22], unlike the original BCS model at $J = 0$, this equation leads to a J-T diagram in which the SC transition can be discontinuous in Δ, i.e., of first order. Below the temperature $T/T_{c0} \approx 0.6$ at point A, i.e., below the dashed line in Fig. 3(b), no small Δ solution to the nonlinear equation can be found and the initial assumption of the linearization that an arbitrarily small solution exists is not valid.

While we can find a nonvanishing solution Δ, it may not correspond to the stable thermodynamic phase. In Fig. 3(b), we remove the nonvanishing solutions Δ, if the free energy favors the magnetic state. The resulting T-J diagram shows that for J larger than the Chandrasekhar-Clogston limit at $T = 0$ [20,21] of $J_c = \Delta_0/\sqrt{2}$, no SC solution is stable.

Another interesting approach to describe SC in the presence of a magnetic field is presented by Powell *et al.* [22] who use a Hubbard model in connection with a homogeneous exchange splitting. They treat the pairing part of the interactions among electrons in the system in the Hartree-Fock approximation, similar to BCS as described above and consequently arrive at a similar gap equation as compared to Eq. (5). The matrix elements of the KS system of SpinSCDFT within the spin decoupling approximation will turn out to have a similar analytic structure.

Also, Ref. [22] discusses why the transition is of first order. They observe that for $J < \Delta$ and $T = 0$, the gap equation (5), and consequently Δ, is independent on J. Thus, $\Delta(J) = \Delta_0$ as long as $J < \Delta_0$. If instead we allow for $J > \Delta$ in the range where $\varepsilon < \sqrt{J^2 - \Delta^2}$ the Fermi functions in Eq. (5) are equal and thus cancel at $T = 0$. This solution intersects $\Delta(J) = \Delta_0$ at $J = \Delta$ and corresponds to the unfavorable total energy [14]. At this point follows that $\Delta(T = 0\ \mathrm{K}, J) = \Delta_0\theta(\Delta_0 - J)$ and the transition is discontinuous $T = 0$ in Δ.

The above analysis will be crucial later, in Secs. IV and V, to guide the discussion of the more sophisticated approaches, that feature a qualitatively similar behavior. In the next section, we will discuss results of the Eliashberg method (as derived in Paper I, Sec. IV) when applied to our test system of Sec. II.

IV. SOLUTIONS TO THE PHONON-ONLY ELIASHBERG EQUATIONS

We solve the Eliashberg equations [Paper I, Eqs. (140) to (143)]. The approximations used here, for the special case of a homogeneous exchange field, lead to equations similar to those derived by Vonsovsky *et al.* [13].

Similar to every equation that describes a spontaneously broken symmetry, in addition to a possible finite solution, the Eliashberg equations [Paper I, Eqs. (140) to (143)] always have the solution $\Delta_n^{\mathrm{E}}(J) = 0$. Usually, this non-SC solution is not stable below T_c in the sense that small symmetry-breaking fields (that in the self-consistent iteration scheme are equivalent to a small but nonzero starting guess) lead to the finite $\Delta_n^{\mathrm{E}}(J)$ solution via iteration of the Eliashberg equations [Paper I, Eqs. (140) to (143)]. Thus, we say that in this case the $\Delta_n^{\mathrm{E}}(J) = 0$ solution has a zero basin of attraction; only the starting value $\Delta_n^{\mathrm{E\ init}}(J) = 0$ leads to the final solution $\Delta_n^{\mathrm{E}}(J) = 0$. Whenever $J = 0$, the $\Delta_n^{\mathrm{E}}(J) = 0$ solution has a zero basin of attraction below T_c.

From Eq. (122) in Paper I we know that the complex Δ_n^{E} changes the poles of the Green function (GF). We assume the term $\tilde{A}_k^{\omega}(\omega_n)$ to be zero, for simplicity. Then, from the analytic continuation to the real axis of Eq. (123) in Paper I, we see that the energy ω of such a pole satisfies the condition $\omega = \mathrm{sign}(\sigma)J_k \pm \sqrt{{\varepsilon_k}^2 + \Delta(\omega)^2}$ which is analogous to the usual Eliashberg equations (compare also Ref. [23]). At $T = 0$, the analytic continuation of Δ_n^{E} the real axis is purely real in the range of the Fermi energy and its value there defines the SC excitation gap [23]. Thus, the Matsubara component $n = 0$ of Δ_n^{E} is related to the SC excitation gap of the quasiparticle system. We choose this as a characteristic property that we investigate as a function of J and T. In the following, we generate two J-T diagrams shown in Fig. 4. In Fig. 4(a) we follow the SC solution, i.e., we take the converged $\Delta_n^{\mathrm{E}}(J)$ as input for the calculation at $\Delta_n^{\mathrm{E}}(J + dJ)$, starting at $J = 0$ with dJ positive. This way we compute the diagram "from left to right" and test the stability of the $\Delta_n^{\mathrm{E}}(J) \neq 0$ solution. In Fig. 4(b), we take the converged $\Delta_n^{\mathrm{E}}(J)$ as input for the calculation at $\Delta_n^{\mathrm{E}}(J - dJ)$, starting at $J = 0.5$ mHa. Thus, we generate the diagram "from right to left." Because for large

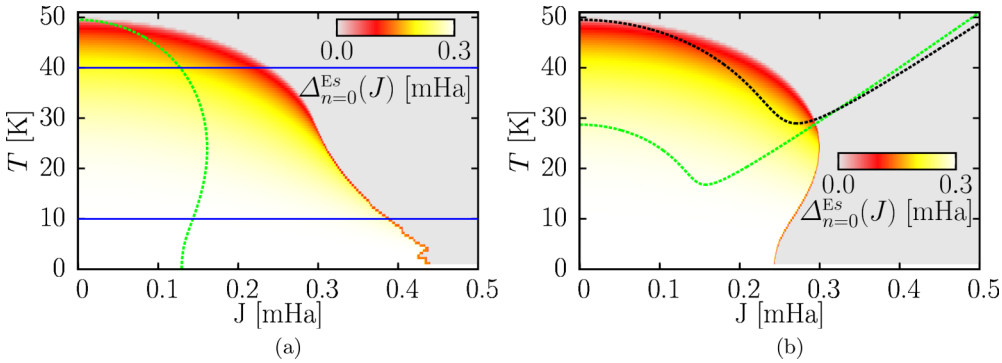

FIG. 4. (Color online) J-T diagram of the $n = 0$ component $\Delta^{E}_{n=0}$ from the solution to the Eliashberg equations. We follow the SC solution $\Delta^{E}_{n}(J) \neq 0$ in (a) or the non-SC solution $\Delta^{E}_{n}(J) = 0$ in (b) and observe that we can find a region where both are (meta)stable. We show the full solution $\Delta^{E}_{n}(J)$ along the blue lines in Fig. 5. For comparison, we show the linear BCS curve as a green dotted line in (a). In (b) we compare with SpinSCDFT results of Sec. V (green curve); the black curve is scaled on both axes by $T_c^{\text{Eliashberg}}/T_c^{\text{SpinSCDFT}}$.

J, $\Delta^{E}_{n}(J)$ is zero, we start from a small, symmetry-breaking value at $\Delta^{E}_{n}(J - dJ)$ instead of zero. This way, we test the stability of the trivial $\Delta^{E}_{n}(J) = 0$ solution.

Comparing Figs. 4(a) and 4(b) we see that the borders of stability between the stability of $\Delta^{E}_{n}(J) = 0$ and $\Delta^{E}_{n}(J) \neq 0$ do not agree. In fact, we find a region where both the $\Delta^{E}_{n}(J) = 0$ and the $\Delta^{E}_{n}(J) \neq 0$ solutions have a finite basin of attraction; here the normal and the SC states are (meta)stable. The shape of the border of the region where $\Delta^{E}_{n}(J) = 0$ is unstable resembles closely to the linear BCS solution which we show in Fig. 4(a) as a green dashed line.

We plot the $\Delta^{E}_{n}(J)$ at $T = 10$ K in Fig. 5(a) and 40 K in Fig. 5(b) as a function of J on the vertical axis. The corresponding equal temperature lines are blue in Fig. 4. We find that the shape is largely independent on the splitting J and the temperature T except for a scale factor. Thus, $\Delta^{E}_{n=0}$ is sufficient to investigate the behavior of the theory. For low temperatures, the downscaling is much less pronounced and it is safe to say that the pairing is almost unaffected by the presence of a splitting up until the point where the SC phase is suppressed. For a high temperature, instead, the downscaling is more pronounced and the transition becomes continuous above a certain temperature.

V. RESULTS OF SPINSCDFT WITH THE $G0$ FUNCTIONAL

In this section, we discuss the numerical solution of the SpinSCDFT gap equation [Eq. (103) in Paper I] using the xc potential derived in Sec. III C of Paper I. We refer to this functional as the $G0$ functional.

In Eq. (103) of Paper I, we have derived the gap equation of SpinSCDFT using the $G0$ functional. This equation (103), in turn, is derived from the Sham-Schlüter equation for a superconductor, written in Paper I in the form

$$\int d\mathfrak{e}' S_\beta[\Delta^{s}_{S}](\mathfrak{e},\mathfrak{e}')\Delta^{s}_{S}(\mathfrak{e}') = 0. \tag{6}$$

From the previous discussion in Secs. III and IV, a continuous transition is to be expected for a small exchange field intensity J as compared to the transition temperature.

For the point of the continuous transition, Eq. (6) can be linearized in Δ^{s}_{S}. Similar to I, we use the notation with a breve to indicate linearized entities $\breve{S}_\beta = S_\beta[\Delta^{s}_{S} = 0]$. Thus, in this case $T_c(J)$ can be computed from the condition that $\breve{S}_\beta = \breve{S}^{\mathfrak{e}}_\beta + \breve{S}^{M}_\beta + \breve{S}^{\mathfrak{D}}_\beta$ has a singular eigenvalue

$$\det \breve{S}_\beta = 0\,. \tag{7}$$

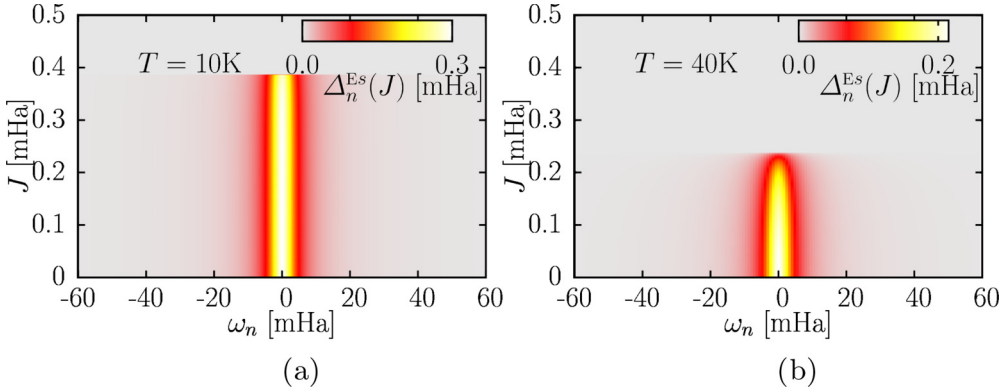

FIG. 5. (Color online) Solutions to the Eliashberg equations $\Delta^{E}_{n}(J)$ for $T = 40$ K (a) and $T = 10$ K (b) along the blue lines of the left panel of Fig. 4.

The corresponding shape of the solution $\Delta_s^s/||\Delta_s^s||$ is the right eigenfunction to such a singular eigenvalue.

The contributions to $\breve{S}_\beta(\mathfrak{e},\mathfrak{e}')$ are given in Eqs. (99)–(102) of Paper I. To investigate the structure and properties of the SpinSCDFT xc potential is easier within the linearized form since the matrix $\breve{S}_\beta(\mathfrak{e},\mathfrak{e}') = \breve{S}^{\mathfrak{e}}_\beta(\mathfrak{e},\mathfrak{e}') + \breve{S}^{\mathrm{M}}_\beta(\mathfrak{e},\mathfrak{e}') + \breve{S}^{\mathfrak{D}}_\beta(\mathfrak{e},\mathfrak{e}')$ is independent of the potential Δ_s^s. As discussed in detail in I, $\breve{S}^{\mathfrak{D}}_\beta(\mathfrak{e},\mathfrak{e}')$ $[\breve{S}^{\mathfrak{e}}_\beta(\mathfrak{e},\mathfrak{e}')]$ corresponds to the Nambu (off-) diagonal self-energy contribution. $\breve{S}^{\mathrm{M}}_\beta$ is due to the v_{xc} part of the Sham-Schlüter equation. In Sec. V A, we present and discuss the shape of the contributions $\breve{S}^{\mathrm{M}}_\beta(\mathfrak{e},\mathfrak{e}')$, $\breve{S}^{\mathfrak{D}}_\beta(\mathfrak{e},\mathfrak{e}')$, $\breve{S}^{\mathfrak{e}}_\beta(\mathfrak{e},\mathfrak{e}')$, and the $T_c(J)$ curve from the linearized xc potential.

Finally, the properties of the general nonlinear gap equation, i.e., the J-T diagram of the solutions to Eq. (6) with and without the Coulomb repulsion, will be presented in Sec. V B.

A. Linearized Sham-Schlüter equation

As discussed before, in the part of the J-T diagram for a relatively small applied field (i.e., low splitting J and high T) we expect a second-order phase transition. This section deals with the corresponding continuous transition. In Sec. V A 1, will show the shape of $\breve{S}^{\mathfrak{e}}_\beta$, $\breve{S}^{\mathrm{M}}_\beta$, and $\breve{S}^{\mathfrak{D}}_\beta$. To determine the point of the transition according to Eq. (7), in Sec. V A 2 we investigate the spectrum of $\breve{S}_\beta$ as a function of temperature and splitting and the corresponding solutions $\Delta_s^s/||\Delta_s^s||$. Then, we will discuss the shape of the $T_c(J)$ curve in Sec. V A 3 from this linear approach.

1. *Temperature dependence of* $\breve{S}_\beta$

The three contributions to $\breve{S}_\beta(\mathfrak{e},\mathfrak{e}')$ are [see Sec. III C 1 of Paper I, Eqs. (99)–(102)]

$$\breve{S}_\beta(\mathfrak{e},\mathfrak{e}') = \left[\breve{S}^{\mathfrak{D}}_\beta(\mathfrak{e}) + \breve{S}^{\mathrm{M}}_\beta(\mathfrak{e})\right]\delta(\mathfrak{e}-\mathfrak{e}') + \breve{S}^{\mathfrak{e}}_{\mathrm{ph}\beta}(\mathfrak{e},\mathfrak{e}') + \breve{S}^{\mathfrak{e}}_{\mathrm{C}\beta}(\mathfrak{e},\mathfrak{e}'). \tag{8}$$

The linear version of the Sham-Schlüter equation (6) is obtained by multiplying the above equation with $\Delta_s^s(\mathfrak{e}')$ and integrating over $\mathfrak{e}'$ with the result $\int d\mathfrak{e}'\breve{S}_\beta(\mathfrak{e},\mathfrak{e}')\Delta_s^s(\mathfrak{e}') = 0$. Thereby, we see that $\breve{S}^{\mathrm{M}}_\beta(\mathfrak{e})$ and $\breve{S}^{\mathfrak{D}}_\beta(\mathfrak{e})$ multiply $\Delta_s^s(\mathfrak{e})$ directly without integration . They are shown for several T for $J = 0.0$ and 0.1 mHa in Figs. 6(a) and 6(b), respectively. Note the logarithmic center-of-energy ε scale in all the plots in this section. The color scale blue to red indicates increasing temperatures. All terms have features only in the close vicinity to $\varepsilon = 0$ and quickly decay to zero within a characteristic energy width of the phonon coupling. This energy scale is the analog of Debye frequency ω_0 in Eq. (2). However, the ε dependence shown in Fig. 6 in the presence [panel (b)] and the absence [panel (a)] of an exchange splitting is very

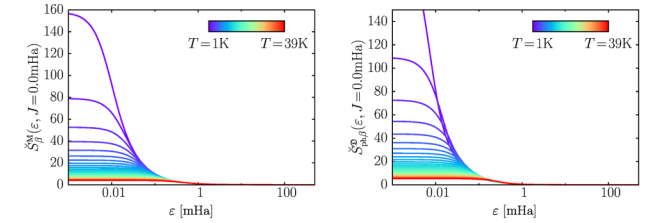

(a) $\breve{S}^{\mathrm{M}}_\beta(\mathfrak{e})$ (l.) and $\breve{S}^{\mathfrak{D}}_\beta(\mathfrak{e})$ (r.) for $J = 0$mHa

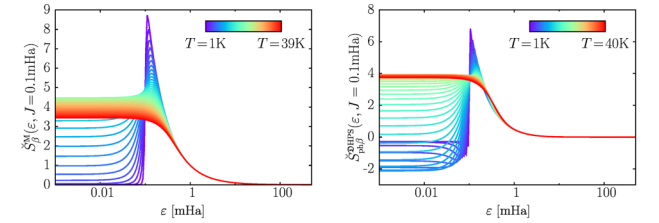

(b) $\breve{S}^{\mathrm{M}}_\beta(\mathfrak{e})$ (l.) and $\breve{S}^{\mathfrak{D}}_\beta(\mathfrak{e})$ (r.) for $J = 0.1$mHa.

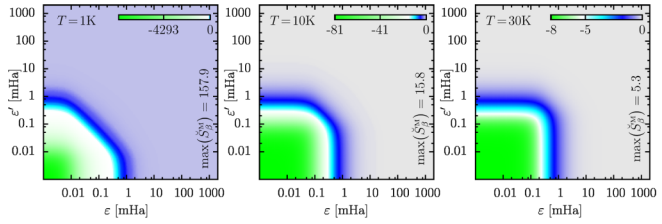

(c) $\breve{S}^{\mathfrak{e}}_{\mathrm{ph}\beta}(\mathfrak{e},\mathfrak{e}')$ for $J = 0.0$mHa at (l. to r.) $T = 1\mathrm{K}, 10\mathrm{K}, 30\mathrm{K}$

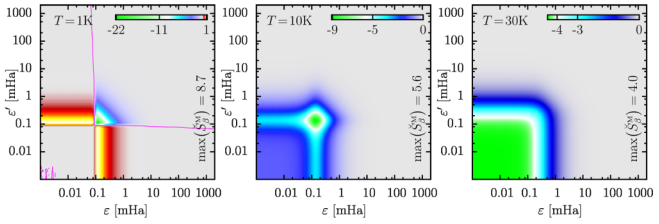

(d) $\breve{S}^{\mathfrak{e}}_{\mathrm{ph}\beta}(\mathfrak{e},\mathfrak{e}')$ for $J = 0.1$mHa at (l. to r.) $T = 1\mathrm{K}, 10\mathrm{K}, 30\mathrm{K}$

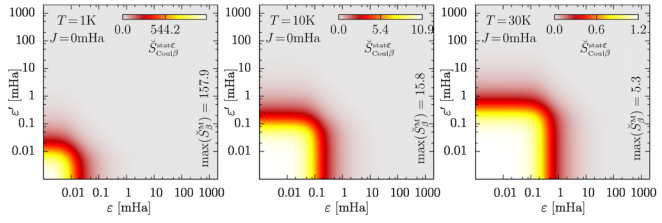

(e) $\breve{S}^{\mathfrak{e}}_{\mathrm{C}\beta}(\mathfrak{e},\mathfrak{e}')$ for $J = 0.0$mHa at (l. to r.) $T = 1\mathrm{K}, 10\mathrm{K}, 30\mathrm{K}$

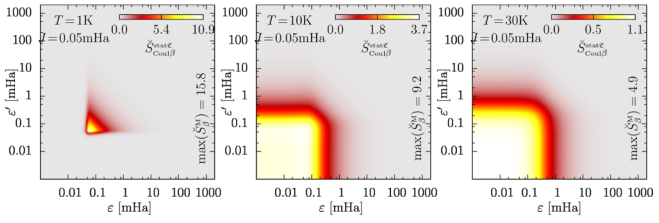

(f) $\breve{S}^{\mathfrak{e}}_{\mathrm{C}\beta}(\mathfrak{e},\mathfrak{e}')$ for $J = 0.05$mHa at (l. to r.) $T = 1\mathrm{K}, 10\mathrm{K}, 30\mathrm{K}$

FIG. 6. (Color online) Contributions to the linearized Sham-Schlüter equation (6). In the top row, we show the diagonal $\breve{S}^{\mathrm{M}}_\beta$ and $\breve{S}^{\mathfrak{D}}_\beta$ that originate from the v_{xc} and Nambu diagonal self-energy in the Sham-Schlüter equation, respectively. In the second (bottom) row, we show the contributions that originate from the Nambu off diagonal phonon (Coulomb) self-energy. The color scale of $\breve{S}^{\mathfrak{e}}_\beta(\mathfrak{e},\mathfrak{e}')$ for negative values (decreasing: blue to white to green) is relative to $\max(\breve{S}^{\mathrm{M}}_\beta)$ (white). Red to yellow to white indicates increasingly positive values. Note that $\breve{S}^{\mathfrak{D}}_\beta$ and $\breve{S}^{\mathfrak{e}}_{\mathrm{ph}\beta}$ switch sign at $\varepsilon \approx 0$ for $J = 0.1$ mHa at low T as compared to $J = 0$ mHa.

different. In fact, in Fig. 6(a) where $J = 0$ both $\check{S}^{\mathrm{M}}_{\beta}(\mathfrak{e})$ and $\check{S}^{\mathfrak{D}}_{\beta}(\mathfrak{e})$ are positive and monotonously decreasing as a function of $|\varepsilon|$. In presence of a $J \neq 0$ [Fig. 6(b)], instead, they have the following complex temperature and energy dependence: For small T in the range $|\varepsilon| < J$, $\check{S}^{\mathfrak{D}}_{\beta}(\mathfrak{e})$ is negative and, in the limit $T \to 0$, $\check{S}^{\mathrm{M}}_{\beta}(\mathfrak{e})$ and $\check{S}^{\mathfrak{D}}_{\beta}(\mathfrak{e})$ approach zero from opposite sides. At $|\varepsilon| \approx J$, both $\check{S}^{\mathrm{M}}_{\beta}(\mathfrak{e})$ and $\check{S}^{\mathfrak{D}}_{\beta}(\mathfrak{e})$ vary very rapidly. This behavior is smoothed out with increasing T and at temperatures high enough with respect to J the nonsplitted behavior is recovered. The temperature dependencies at $J = 0$ and 0.1 mHa of $\check{S}^{\mathfrak{e}}_{\mathrm{ph}\beta}(\mathfrak{e},\mathfrak{e}')$ are shown in Figs. 6(c) and 6(d), respectively. $\check{S}^{\mathrm{M}}_{\beta}$ serves as a scale that other kernel contributions have to be compared with, so we choose a color scale relative to the maximum of $\check{S}^{\mathrm{M}}_{\beta}$, indicated on the right of every plot.

For $J = 0$ mHa we note that the size of $\check{S}^{\mathfrak{e}}_{\mathrm{ph}\beta}(\mathfrak{e},\mathfrak{e}')$ [Fig. 6(c)] decays faster with temperature than the size of the diagonal $\check{S}^{\mathrm{M}}_{\beta}$ and $\check{S}^{\mathfrak{D}}_{\beta}$. This can be seen from the the position of "white" in the color scale of Fig. 6(c) which moves to the left with increasing temperatures. Furthermore, being both positive and diagonal, $\check{S}^{\mathrm{M}}_{\beta}$ and $\check{S}^{\mathfrak{D}}_{\beta}$ have to be compared with the eigenvalues of $\check{S}^{\mathfrak{e}}_{\mathrm{ph}\beta}$. $\check{S}^{\mathrm{M}}_{\beta}$ and $\check{S}^{\mathfrak{D}}_{\beta}$ alone would result in a positive-definite Sham-Schlüter matrix for $J = 0$ mHa at all temperatures, as can be seen in Fig. 6(a), so there is no nontrivial solution to Eq. (6). Thus, technically, the phase transition from the SC to the non-SC state is induced by this relative reduction of $\check{S}^{\mathfrak{e}}_{\mathrm{ph}\beta}$ as compared to $\check{S}^{\mathrm{M}}_{\beta}$ plus $\check{S}^{\mathfrak{D}}_{\beta}$. We will turn to a systematic analysis of the eigenvalues of the linearized Sham-Schlüter matrix $\check{S}_{\beta}$ in Sec. V A 2.

The relative scale reduction is also found for the splitted $\check{S}^{\mathfrak{e}}_{\mathrm{ph}\beta}$. At $\varepsilon \approx 0$, however, we stay much below the scale of $\check{S}^{\mathrm{M}}_{\beta}$ and exceed it only for higher temperatures. Moreover, the sign change of $\check{S}^{\mathfrak{D}}_{\beta}$ is effectively reducing the diagonal repulsion.

A purple line in Fig. 6(d) indicates the zero contour and shows that for very low T, $\check{S}^{\mathfrak{e}}_{\mathrm{ph}\beta}(\mathfrak{e},\mathfrak{e}')$ is positive for approximately the region where $|\varepsilon| < J$ or $|\varepsilon'| < J'$ and has a sharp negative peak at $\varepsilon = \varepsilon' \approx J$. Thus, as a curious fact, the phonon interaction is not "attractive" everywhere in this case. We show the shape of the static Coulomb part $\check{S}^{\mathfrak{e}}_{C\beta}$ in Figs. 6(e) and 6(f) for $J = 0$ and 0.05 mHa, respectively. Apart from the differences in sign, the overall behavior of the Coulomb term and phonon terms is roughly similar with significant deviations in the fact that it does not change sign for a low temperature and exchange splitting [compare Fig. 6(d) with 6(f)].

In summary, we can say that we see relevant changes in the shape of the contributions to $\check{S}_{\beta}$ for a finite exchange splitting for the low-temperature limits in the region $|\varepsilon| < |J|$ as compared to the spin degenerate case. At higher temperatures, the splitting becomes less important. We point out that we know from the earlier discussion that this is the region, where we expect the linearization to be unjustified. From the form of the Bogoliubov eigenvalues $E^{\sigma}_{\alpha} = \mathrm{sign}(\sigma)J + \mathrm{sign}(\alpha)\sqrt{\varepsilon^2 + |\Delta^{\mathrm{s}}_{\mathrm{s}}|^2}$ we expect that, whenever $\Delta^{\mathrm{s}}_{\mathrm{s}}$ is larger than J, will see a behavior more similar to the case $J = 0$. The reason is that, then, only the $\alpha = +$ branch has positive excitation energies $E^{\sigma}_{+} \geqslant 0$, meaning that the ground state does not correspond to some of the excitations $\hat{\gamma}_k$ being occupied. For details, see the discussion in Sec. III A 2 d of Paper I and in Ref. [14].

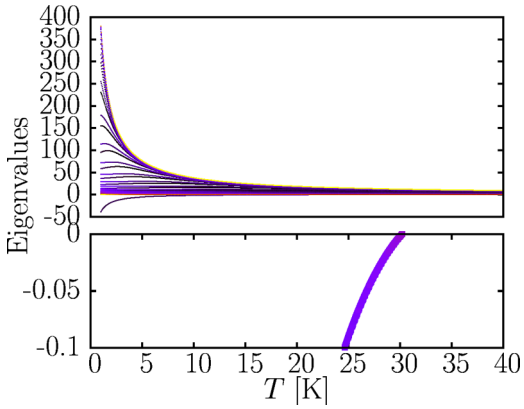

FIG. 7. (Color online) Spectrum of $\check{S}_{\beta}(J = 0.0$ mHa) as a function of T with only one negative eigenvalue that leads to a singular point.

2. *Critical temperatures and the shape of $\Delta^{\mathrm{s}}_{\mathrm{s}}$ the pair potential*

Since we compute the critical temperature from Eq. (7), i.e., the occurrence of a singular eigenvalue of $\check{S}_{\beta}$, in this section, we will investigate the full spectrum of $\check{S}_{\beta}$ as a function of T and J.

The KS potential $\Delta^{\mathrm{s}}_{\mathrm{s}}$ is proportional to the right eigenvector of $\check{S}_{\beta}$ that is associated to a singular eigenvalue. Thus, all eigenfunctions $\Delta^{\mathrm{s}}_{\mathrm{s}}$ we show are normalized to a common arbitrary value. In this section, we are not considering the Coulomb contribution. We show the spectrum of $\check{S}_{\beta}$ as a function of temperature in Fig. 7. In the spin degenerate case $J = 0$ mHa, we see that the eigenvalues decrease in magnitude with temperature in a monotonous way. At low temperature, all eigenvalues but one are positive; the negative eigenvalue crosses zero at the temperature $T_{\mathrm{c}}(J = 0$ mHa$) \approx 30$ K in the present system, above which $\check{S}_{\beta}$ becomes positive definite. The temperature at which the crossing occurs is the critical temperature.

As compared to the $J = 0$ mHa, the spectrum at finite splitting $J = 0.1$ mHa shown in Fig. 8 is fundamentally different. For small T, we observe many negative eigenvalues and, most interestingly, several solutions $\det(\check{S}_{\beta}) = 0$ at low

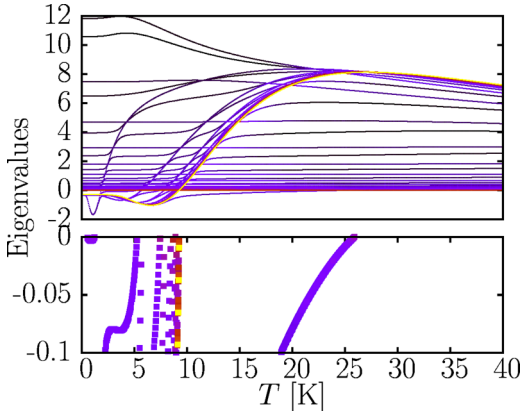

FIG. 8. (Color online) Spectrum $\check{S}_{\beta}(J = 0.1$ mHa) as a function of T with many negative eigenvalues that cross zero and lead to singular points.

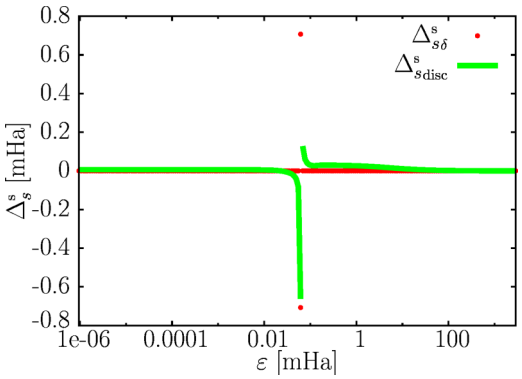

FIG. 9. (Color online) Eigenfunctions to a singular eigenvalue at $T \approx T_{\mathrm{cross}}$. All eigenfunctions except one are of either type.

temperatures. There is a temperature regime $T_{\mathrm{cross}} \approx 10$ K in this system, in which most negative eigenvalues cross zero and become positive. Beyond T_{cross}, only one negative eigenvalue remains that is crossing at a higher temperature $T_c(J = 0.1\ \mathrm{mHa}) \approx 25$ K. Continuously reducing the splitting, this specific eigenvalue/eigenfunction pair can be traced to the spin degenerate limit. Similarly, upon reducing the splitting, it is found that the temperature range where the crossings appear goes to $T_{\mathrm{cross}} \to 0$ K as $J \to 0$.

We analyze the eigenfunctions in Figs. 9 and 10 corresponding to these multiple solutions and see that only the one at $T \approx 25$ K has a continuous behavior. The other solutions are of two kinds shown in Fig. 9 and both show numerical discontinuities. While the green dashed solution in Fig. 9 has a $1/\varepsilon$-like pole, there is a second kind, red in Fig. 9, which has a delta-peak-like structure, i.e., the value at the pole of the first kind is large while the rest is extremely small. Increasing the number of sampling points increased the relative value at the discontinuity, so this led us to the conclusion that we are numerically sampling an unbound function. It has to be understood that an unbound function cannot be the linearized solution to an originally nonlinear fixed-point problem. This is because, at the pole, the function is not small and a linearization cannot be justified. We expect that in the nonlinear equation these types of solutions will be suppressed. We therefore ignore these other, unbound, solutions in the following discussion and always refer to the continuous, bound, high-temperature solution.

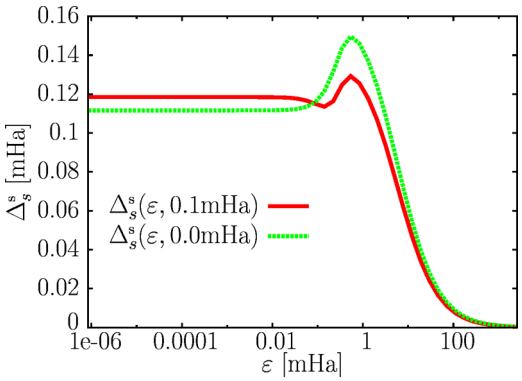

FIG. 10. (Color online) $\Delta^s_s(\mathfrak{e})$ at T_c for $J = 0.0$ and 0.1 mHa without the Coulomb interaction.

As a side remark, we point out that comparing $T_c^{\mathrm{SCDFT}}(J = 0) \approx 30$ K with the solution to the Eliashberg equations, the latter predicts a much higher $T_c^{\mathrm{Eliash}}(J = 0) \approx 50$ K. For a detailed comparison, see Fig. 4(b) where we show the linearized $T_c^{\mathrm{SCDFT}}(J)$ in the phase diagram of the Eliashberg equations. We also observe via the black curve of Fig. 4(b) that the Eliashberg solutions predict a SC phase that is less susceptible against a splitting. The reason for the lower T_c prediction is that within the xc potential construction $\bar{G}$ was replaced with $\bar{G}^{\mathrm{KS}}$ which violates Migdal's theorem [11]. The solution has been recently presented by Sanna *et al.* [24] using a corrected self-energy in the functional construction. We will come back to this point and elaborate on the distinction in the Appendix A. As a curious result, the linearized $T_c^{\mathrm{SCDFT}}(J)$ curve bends upwards and starts an almost linear increase at the point where the transition is expected to become of discontinuous type. We investigate this issue in Sec. V A 3 and give an explanation in Sec. V C after studying the nonlinear gap equation.

3. *Analysis of the B_0 dependence of T_c*

Using the condition of $\check{S}_\beta$ to be positive definite, we compute the $T_c(J)$ curve of the system shown in Fig. 11(a). At a low field, the $T_c(J)$ curve behaves as expected; the critical temperature is slowly reducing with increasing J. Similar to the Eliashberg results in Sec. IV, the SpinSCDFT pair potential seems to be more resistant against a splitting than the BCS approach predicts.

In the regime of a first-order phase transition, where the conditions for a linearization are not met, SpinSCDFT behaves differently as compared to the linear BCS solution of Fig. 3. While in neither case, BCS nor SpinSCDFT, a linearization can be expected to yield sensible results for a discontinuous first-order transition, the behavior of the $T_c(J)$ curve from SpinSCDFT is certainly more unphysical. At high field, past $J \approx 0.15$ mHa in the present system, the $T_c(J)$ curve bends outwards and starts an almost linearly increase with J.

In Fig. 11(b), the eigenfunctions to the singular eigenvalues of $\check{S}_\beta$ for increasing J are plotted. We can clearly observe that the upturn of the $T_c(J)$ curve is accompanied by an increasing localization of Δ^s_s at the Fermi level. The usual high-energy tail gets more and more suppressed. For very large splittings, Δ^s_s becomes numerically noisy. Reintroducing the Coulomb coupling in S_β, apart from the expected reduction of T_c, we observe a similar behavior, with the unphysical increase of $T_c(J)$ in Fig. 11(c) for large J. In this case, Δ^s_s plotted in Fig. 11(d) shows a characteristic negative tail induced by the Coulomb renormalization mechanism [25,26] as it occurs within SCDFT [11,12,18]. We will come back to the increase of $T_c(J)$ later in Sec. V C. As a second point, we note that in the regime of the continuous transition, where a linearization is sensible, the SpinSCDFT and the BCS $T_c(J)$ deviate. From the comparison between $T_c^{\mathrm{SpinSCDFT}}(J)$ with the green dashed BCS curve in Fig. 11(a), we note that in the second-order regime $T_c^{\mathrm{BCS}}(J)$ scales down with J faster. In order to make the strong coupling SpinSCDFT theory more similar to the weak coupling BCS approach, we disregard $\check{S}^{\mathfrak{D}}_\beta$ in Figs. 11(e) and 11(f). In this case, we are only considering the effectively attractive coupling among electrons via phonons, similar to Fröhlich [27] and BCS.

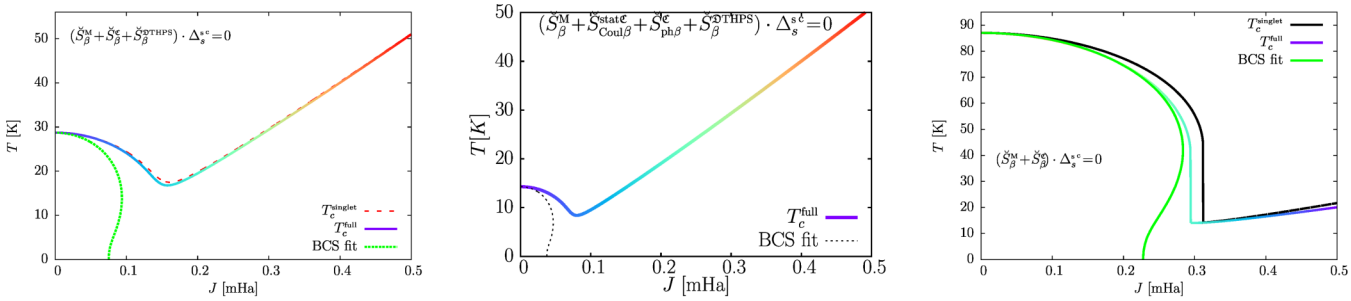

(a) $T_c(J)$ excluding the Coulomb coupling and removing triplet self-energy parts (singlet) or not (full) plus a BCS fit to the same $T_c(J=0)$.

(c) $T_c(J)$ including the Coulomb coupling together with a BCS fit to the same $T_c(J=0)$.

(e) $T_c(J)$ excluding the Coulomb coupling and $\breve{S}^{\mathfrak{D}}_\beta$ together with the linear BCS curve.

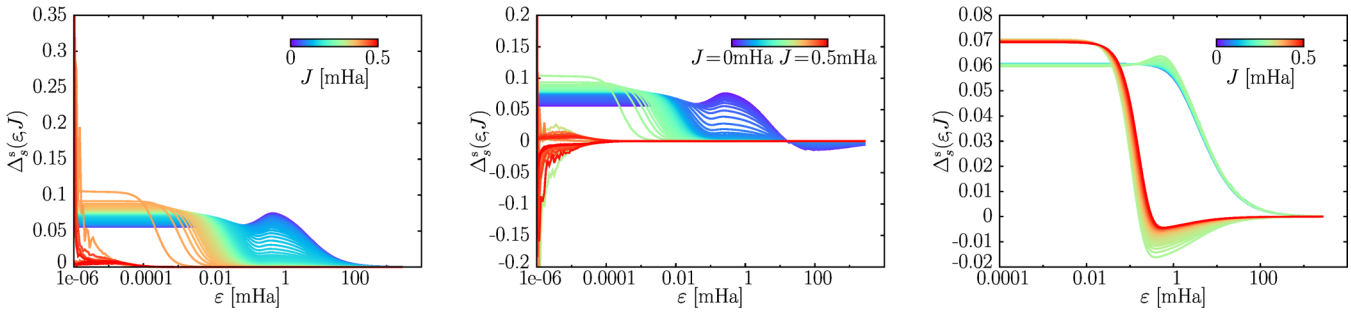

(b) Normalized $\Delta^s_s(\mathfrak{e})$ at $T_c^{\text{full}}(J)$ of (a).

(d) Normalized $\Delta^s_s(\mathfrak{e})$ at $T_c^{\text{full}}(J)$ of (c).

(f) The normalized $\Delta^s_s(\mathfrak{e})$ from $\breve{S}_\beta - \breve{S}^{\mathfrak{D}}_\beta$ at $T_c(J)$ of (e).

FIG. 11. (Color online) $T_c(J)$ from SpinSCDFT and the linear BCS curve with the same $T_c(J=0)$. We show the $T_c(J)$ in, or excluding the Coulomb coupling in, or excluding contributions from triplet self-energy parts. Beyond the range of the continuous transition, the SpinSCDFT solutions start to increase at $J \approx 0.15$ mHa. This point marks the border of the appearance of the unphysical solutions discussed in Sec. V C. The effect of the Coulomb potential is to reduce the $T_c(J=0)$, but the overall shape remains essentially unaltered. The normalized eigenfunctions are shown with a color code indicating the respective splitting. The solutions become numerically noisy at large splittings.

The effective Fröhlich interaction requires the coupling to be small, and moreover we neglect the phonon influence on the normal state via the Nambu diagonal part of the self-energy entirely. Thus, this approximation is called the weak coupling limit. As expected, the resulting $T_c^{\text{SpinSCDFT}}(J)/T_c^{\text{SpinSCDFT}}(0)$ and $T_c^{\text{BCS}}(J)/T_c^{\text{BCS}}(0)$ behave very similarly. Here, the $T_c(J)$ curves shown in Fig. 11(e) also feature the linear increase for high splitting. Moreover, we observe a discontinuous jump of the critical temperature at a certain splitting J_c which is accompanied by the eigenfunction dramatically changing shape. After the jump, the solution does not have a common sign convention but shows positive and negative parts. Also, here we find numerically noisy solutions.

The BCS $T_c(J)$ curve, fitted to the same $T_c(0$ mHa), matches the weak coupling SpinSCDFT $T_c(J)$ curve Fig. 11(e), not the strong coupling curve of Fig. 11(a). This points out that the strong coupling $\breve{S}^{\mathfrak{D}}_\beta$ term does not simply scale $T_c(J)$ down equally on both T and J axes. Instead, $\breve{S}^{\mathfrak{D}}_\beta$ leads to a larger $T_c(J)$ reduction of the temperature axis. Thus, we conclude that strong coupling systems are less effected by an exchange splitting relative to their $T_c(0$ mHa).

B. Nonlinear Sham-Schlüter equation

The previous section has shown the importance to consider the fully nonlinear Sham-Schlüter equation $S_\beta[\Delta^s_s]\Delta^s_s = 0$ of Eq. (6) when working in the limit of strong external field/large exchange splitting J. We solve the fully nonlinear Sham-Schlüter equation

$$\Delta^s_s = \mathcal{K}_{\mathcal{S}}[\Delta^s_s]\Delta^s_s, \tag{9}$$

$$\mathcal{K}_{\mathcal{S}} = \mathcal{S}^{-1}(S_\beta + \mathcal{S}), \tag{10}$$

with the splitting matrix $\mathcal{S}$ chosen to be $S^M_\beta(\varepsilon, J=0.0$ mHa) Details on this procedure can be found in Sec. III C 2 in Paper I. In Fig. 12 we show results, neglecting the Coulomb coupling along the isosplitting line $J=0.0$ mHa as a function of temperature T. We obtain a $\Delta^s_s(\mathfrak{e})$ that goes to zero at the Fermi level for low temperatures as can be seen by the purple to blue lines in Fig. 12. This means the SC KS system is not gapped while still maintaining $\chi \neq 0$, and we cannot directly interpret the SC KS excitations as quasiparticles.

It is important to highlight that the SC KS system has been constructed to reproduce the density, not the excitation spectrum, so this result, albeit inconvenient for practical purposes, does not invalidate the method. The improved functional for the spin degenerate case by Sanna *et al.* [24] also leads to KS gap that approaches zero at the Fermi level for very small temperatures.

What has to be considered is that one of our approximations in I was to replace the interacting GS with the SC KS GF in

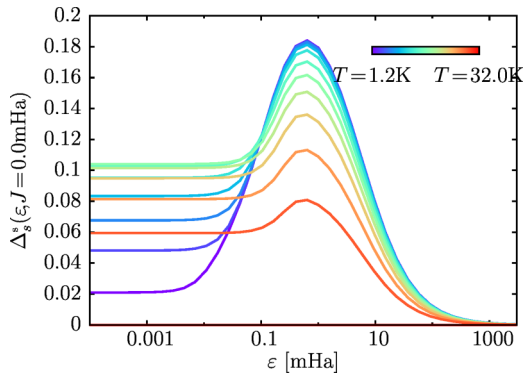

FIG. 12. (Color online) $\Delta_s^s(\epsilon)$ for $J = 0.0$ mHa as a function of T. For low T, $\Delta_s^s(\epsilon)$ goes to zero at $\varepsilon \approx 0$.

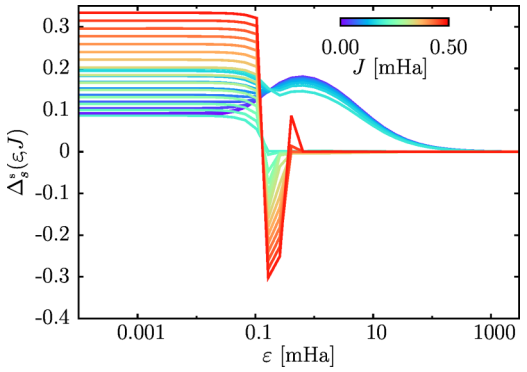

FIG. 14. (Color online) $\Delta_s^s(\epsilon)$ for $T = 10$ K as a function of J. At $J \approx 0.17$ mHa, $\Delta_s^s(\epsilon)$ dramatically change shape.

the self-energy for the functional construction. Being a SC, the interacting GF will be gapped while the SC KS GS may not be. We will come back to this point in Sec. V C where we give an explanation of the upward bending of the SpinSCDFT $T_c(J)$ curve.

In order to have the computationally convenient DFT scheme and a good approximation to the quasiparticle structure at the same time, we introduce the one-cycle Dyson equation iteration for SC in the Appendix A. This approach is similar to the common G_0W_0 approximation in band-structure theory [15] and leads to excellent results in SpinSCDFT.

To complete the discussion of the J and T dependence of SpinSCDFT, we need a characteristic number of a given $\Delta_s^s(\epsilon)$ solution. As mentioned, $\Delta_s^s(\varepsilon = 0, J)$ is not a sensible choice because it neither corresponds to an excitation gap nor is it a measure for the size of the potential $\Delta_s^s(\epsilon)$.

Instead, we chose $\int \Delta_s^s(\epsilon) d\varepsilon$ and the resulting SpinSCDFT J-T diagram of Fig. 13 shows a transition at a point where, from the shape of the nonlinear BCS and Eliashberg diagram, the first-order phase transition is to be expected. However, following this discontinuous transition, the solutions $\Delta_s^s(\epsilon)$ do not vanish but have a different shape. In Fig. 14, we show the $\Delta_s^s(\epsilon)$ with increasing splitting on the equal-temperature line at $T = 10$ K and the transition is clearly seen. In general, while before a critical splitting $J_c(T)$ the potential is little effected by the splitting, past $J_c(T)$ the solutions $\Delta_s^s(\epsilon)$ localize at the Fermi level and show positive as well as negative regions.

This behavior is similar to the shape of the solutions from the linearized $\check{S}_\beta$ as given in Fig. 11(b). We show the $T_c(J)$ curve from the linear equation as a dashed blue line in Fig. 13 and see that it marks the border of the appearance of the curious solutions in the nonlinear equation past the range in J of the second-order phase transition. We show $\Delta_s^s(\epsilon)$ at $J = 0.1$ mHa as a function of T in Fig. 15 noting that its value at $\varepsilon \approx 0$ always remains above J for small temperatures (compare Fig. 12) to prevent the switching of the Bogoliubov branches.

Due to the Coulomb renormalization, including the Coulomb repulsion, $\int \Delta_s^s(\epsilon) d\varepsilon$ is predominantly negative. Thus, as a physical property, we compute the number of condensed electrons $N_{sc} = \int d\boldsymbol{r} \int d\boldsymbol{r}' |\boldsymbol{\chi}(\boldsymbol{r}, \boldsymbol{r}')|^2$ instead of the plain integral. We show the SpinSCDFT J-T diagram including the Coulomb coupling in Fig. 16. The region past the transition has essentially no condensed electrons, while, still, the $\Delta_s^s(\epsilon)$ is not zero as shown in Fig. 17.

C. Origin of the unphysical solutions in the discontinuous regime

The interacting GF, in contrast to the SC KS GF, will be gapped for a SC. Comparing the energy range where the deviation between this two GFs will be the largest, namely $\varepsilon \approx 0.01$ mHa and lower, with the region where the unphysical solutions past the transition (green to red) localize in Fig. 14 we find that these energy ranges coincide. In addition, we

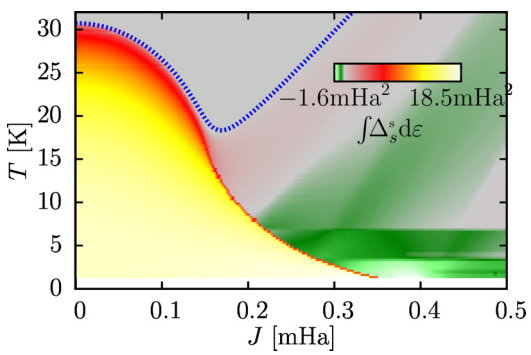

FIG. 13. (Color online) J-T diagram of solutions to the nonlinear gap equation. We include the $T_c^{\text{full}}(J)$ curve (dashed blue) from the linearized functional of Fig. 11(a).

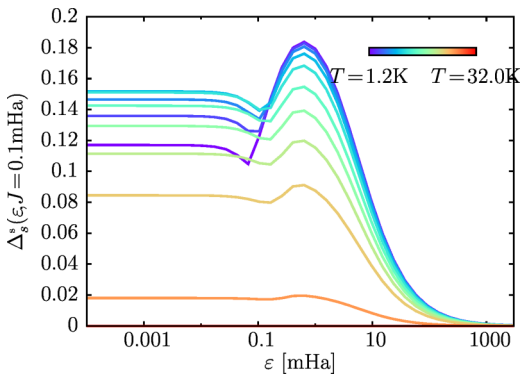

FIG. 15. (Color online) $\Delta_s^s(\epsilon)$ for $J = 0.1$ mHa as a function of T. For low T, $\Delta_s^s(\epsilon)$ remains above J at $\varepsilon \approx 0$.

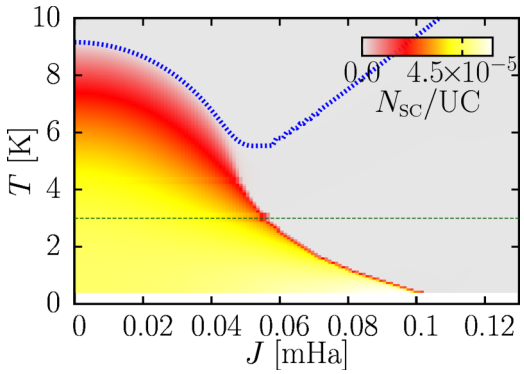

FIG. 16. (Color online) $N_{SC}(T,J)$ and the linear $T_c(J)$ (dashed blue line) including the Coulomb repulsion. The $\Delta_s^s(\mathfrak{e})$ after the transition leads to almost no condensed electrons.

note that at the point of the transition, that corresponds to the light green solutions in Fig. 14 at $J \approx 0.17$ mHa, the value of Δ_s^s at the Fermi level drops below the value of the splitting J. This leads to a swapping of the Bogoliubov particle and hole branch as discussed in Sec. III A 2 d of Paper I which causes severe problems in the construction of the Bogoliubov transformations. Since, thus, the unphysical solutions are characterized by the swapping of the Bogoliubov branches due to $\Delta_s^s(\varepsilon \approx 0) < J$ and we are essentially substituting the true many-body gap with Δ_s^s in the functional construction in I, it is very likely that it is exactly this substitution $G \to G^{KS}$ that causes the appearance of the unphysical solutions in the first place.

D. Numerical calculation of the DOS from the G_0W_0 GF

We compute the GF according to the SC G_0W_0 scheme derived in the Appendix A. In detail, we solve Eq. (A38) using Eqs. (A23)–(A26) together with Eqs. (A2)–(A5) for the model and couplings described in Sec. II. We exclude the Coulomb potential at this point for a better comparison with Eliashberg theory although there is no difficulty to include it.

In Fig. 18, we compute the G_0W_0 corrected DOS at every point in J and T and extract the SC excitation gap. We find that

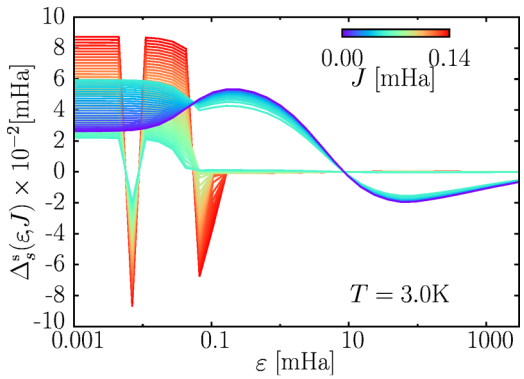

FIG. 17. (Color online) $\Delta_s^s(\mathfrak{e})$ at $T = 3$ K for several J along the dashed green line in Fig. 16. The $\Delta_s^s(\mathfrak{e})$ past the transition at $J = 0.056$ mHa are similarly confined to the Fermi level region as without the Coulomb repulsion.

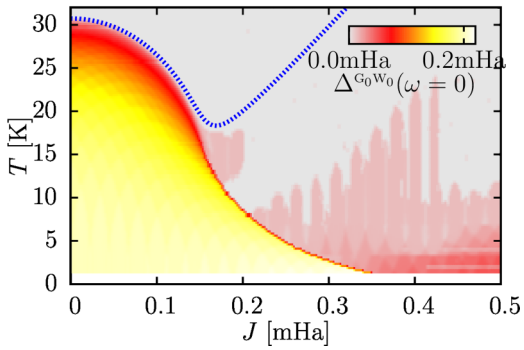

FIG. 18. (Color online) The SC gap in the SpinSCDFT G_0W_0 DOS. The dashed blue line is the linear $T_c^{full}(J)$ of Fig. 11(a).

the curious solutions past the transition $J_c(T)$ lead to almost no excitation gap. The reason is that for the self-energy in the calculation of the SC DOS in the Appendix A, $\Delta_s^s(\mathfrak{e})$ is integrated in ε. In the high-ε region, away from the Fermi level, the contributions to the integral are negligible because the KS potential past $J_c(T)$ is extremely small in this large ε range. Thus, the effect of these solutions Δ_S^s on the G_0W_0 excitation gap is negligible. The ω resolved DOS along the $J = 0$ mHa line and the up and downspin DOS along the $T = 10$ K line of Fig. 18 is shown in Figs. 19(a)–19(c), respectively. The SC G_0W_0 gap including the Coulomb potential is presented in Fig. 20 and similar to the results without the Coulomb interaction of Fig. 18. The ω-resolved DOS for the upspin channel along the thin dashed $T = 3$ K line of Fig. 20 is given in Fig. 21 and, again, we only find small features past the discontinuous transition.

Comparing the SpinSCDFT G_0W_0 gap of Fig. 18 with the BCS (Fig. 3) and the Eliashberg J-T diagram (Fig. 4) we conclude that the point of the transition can be clearly identified. We have seen that for small T and $J = 0$ the nonlinear $\Delta_s^s(\mathfrak{e})$ go to zero at the Fermi level (compare Fig. 12) while the analogous gap from the G_0W_0 GF, the excitation gap of Fig. 18, takes its largest value at $T = 0$ and shows the expected monotonous decay with temperature to T_c.

This implies a significant difference in the quasiparticle states if a splitting occurs with such a $\Delta_s^s(\mathfrak{e})$. While the KS particle with the dispersion $E_\sigma^\alpha = \mathrm{sign}(\sigma)J + \alpha\sqrt{\varepsilon^2 + \Delta_s^s(\mathfrak{e})^2}$ is strongly altered by the splitting because the Bogoliubov branches change their order (compare the earlier discussion in the conclusion of Sec. V A 1 and in I) this is not the case in the true quasiparticle structure. In fact, from Fig. 15, we see that the SC solutions $\Delta_s^s(\mathfrak{e})$ if $J > 0$ do not go to zero and, instead, rise with J to prevent this situation. On the other hand, after the discontinuous transition we find $\Delta_s^s(0,J) < J$.

As discussed before, the replacement $\bar{G} \to \bar{G}^{KS}$ in the functional construction is thus a strong suspect for the occurrence of this curious solution past the SC transition because $\bar{G}$ and $\bar{G}^{KS}$ deviate in that the latter can be nongapped while still corresponding to a SC solution.

E. Triplet components

The present implementation of SpinSCDFT assumes the spin decoupling approximation, i.e., assumes the pairing to

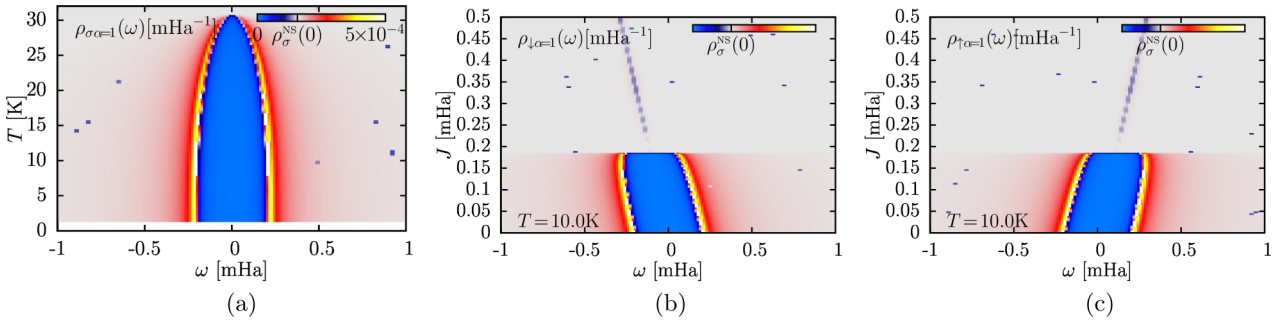

FIG. 19. (Color online) DOS from the G_0W_0 GF. We show the DOS in (a) corresponding to the SpinSCDFT results $\Delta_s^s(\mathfrak{e})$ shown in Fig. 12 for no splitting $J = 0$ mHa. In (b) ($\sigma = \downarrow$) and (c) ($\sigma = \uparrow$) we present the two different spin channels of the DOS with the SpinSCDFT results for the $\Delta_s^s(\mathfrak{e})$ along the isotemperature line $T = 10$ K as shown in Fig. 14.

be of spin-singlet type (compare Sec. III A 2 c of Paper I). However, it was also shown in I that a magnetic splitting creates triplet components in the pairing potential, even for a purely singlet order-parameter density. Triplet components appear as an intermediate step in the self-energy that leads to the $G0$ functional in I since the Nambu off-diagonal up-spin and down-spin components are in general not equal and of opposite sign. They can be intermediate since such triplet self-energy contributions lead to triplet as well as singlet order-parameter contributions. The intermediate triplet self-energy that leads to singlet order-parameter contributions can be included in the spin decoupling approximation functional without difficulties. From the theoretical side, this is an unpleasant signature of formal inconsistency. We have, in fact, computed the critical temperature and KS gaps with and without these intermediate triplet self-energy terms. In Sec. V A 2 and Fig. 11(a) and Fig. 11(e), comparing $T_c(J)$ curves with and without those contributions, we observe that their effect is negligibly small. The possibility of a triplet condensation, i.e., nonvanishing triplet order-parameter contributions, is not investigated further in this work.

F. Extension to real materials

In this work, properties of the free-electron gas with a phonon and Coulomb coupling subject to a homogeneous exchange splitting have been calculated. To compute real materials without the use of adjustable parameters, the electron-phonon coupling and the Coulomb potential have to be calculated from first principles. Then, according to Eqs. (132)–(134) of Paper I these couplings, as well as the computed single-particle states $\varepsilon_{k\sigma}$ may well have a distribution in J different from the homogeneous $J_0 = -\mu_B B_0$ that we are considering here. Also, sometimes several regions in the Brillouin zone (or in k) have different couplings and a different SC pairing as in the well-known case of MgB_2 [28]. The isotropic formulation does not have to be given up; often it is enough to group this region which we refer to as multiband SC [28,29]. We extend notation $\mathfrak{e} = (\varepsilon, J, b)$, $\int d\mathfrak{e} = \int d\varepsilon \int dJ \sum_b$ where b labels the groups of quantum numbers $\{k\}$ sharing similar pairing.

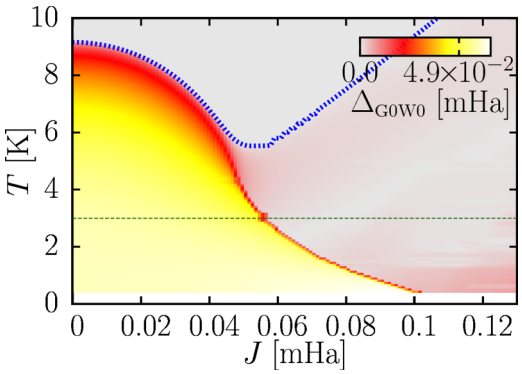

FIG. 20. (Color online) The SC gap in the SpinSCDFT G_0W_0 DOS. The dashed blue line is the linear $T_c^{\rm full}(J)$ of Fig. 11(c).

VI. SUMMARY AND CONCLUSION

In this work, we have presented parameter-free *ab initio* calculations of a superconductor in presence of a homogeneous exchange splitting as, for example, the result of an external magnetic field. We have used two approaches: a generalization of the Eliashberg approach and SpinSCDFT. SCDFT allows the direct inclusion of Coulomb interactions in a straightforward way, while its direct inclusion remains to be problematic within Eliashberg where one has to rely on the $\mu^\star$ approach [25,30]. The Eliashberg equations, on the other hand, provide the reference for the phononic self-energy, allowing to understand and develop functionals for SpinSCDFT.

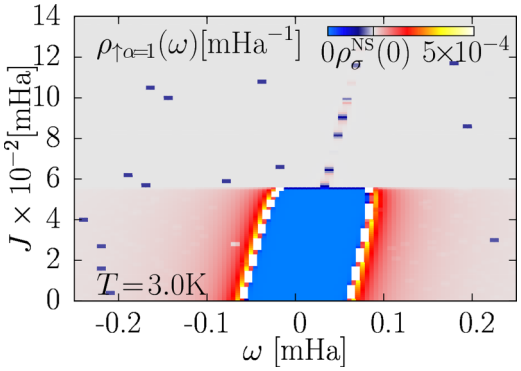

FIG. 21. (Color online) Up-spin channel of the G_0W_0 DOS along the dashed green line in Fig. 20 at $T = 3$ K. We see only small features from the unphysical, oscillatory solutions past the transition (light blue to red in Fig. 17.)

We have implemented a code that solves the SpinSCDFT equations with a linear and nonlinear xc potential and the nonlinear Eliashberg equations derived in I. The xc functional is derived in I from the Sham-Schlüter equation based on the replacement of the interaction with the SC KS GF. We have investigated the behavior of the xc potential on a model of a free-electron gas with a tunable, homogeneous exchange splitting J, a phonon coupling that resembles to the one of MgB_2 and, optionally, a static Coulomb interaction in the Thomas-Fermi approximation. We compute the SC properties of this system and find that in the regime of a second-order phase transition in the T versus J diagram, SpinSCDFT is qualitatively similar to the Eliashberg solutions. In the weak coupling approximation, i.e., removing the contributions in the functional that arise from the normal-state (Nambu diagonal) part of the self-energy, we arrive at a shape that is very similar to the BCS behavior. Including the Coulomb interaction reduces the critical temperature but otherwise does not largely effect the shape of the J-T diagram.

In agreement with BCS and Eliashberg, SpinSCDFT predicts a discontinuous transition in $\Delta_s^s(\mathfrak{e})$ for large J except that the $\Delta_s^s(\mathfrak{e})$ past the transition are not zero but have a curious shape that has positive and negative values. These solutions $\Delta_s^s(\mathfrak{e})$ past the transition increasingly localize at the Fermi level $\varepsilon \approx 0$. In addition and in agreement with the improved functional for SCDFT by Sanna *et al.*, we find that the nonlinear SpinSCDFT solutions go to zero at $\varepsilon \approx 0$ for $T \to 0$ and $J = 0$ and thus the SC KS GF is not gapped while the interacting and G_0W_0 GF is.

The SpinSCDFT solutions past the transition show $|J| > |\Delta_s^s(0, J)|$ and since we have noted in I that it is difficult to construct the Bogoliubov transformations in this case, these solutions are, in fact, unphysical. Since the energy range where the SC KS gap goes to zero agrees with the energy range that causes the unphysical solutions and in our functional construction in I we have substituted the many-body gap with the SC KS gap, we believe that it is this substitution that causes the occurrence of the unphysical solutions in the first place.

We perform a G_0W_0-like correction to the GF where we solve the Dyson equation with the same self-energy that we used originally for the xc-potential construction. The resulting excitation spectrum (here in the isotropic case the DOS) is gapped and behaves as one would expect for a SC. From this result we conclude that a fitting technique of the self-energy similar to Sanna *et al.* [24] will allow us to reproduce the J-T diagram of Eliashberg and remove the unphysical solutions, while keeping the possibility to include the Coulomb potential in addition to a numerically simple form where the Matsubara summations can be computed analytically.

APPENDIX: QUASIPARTICLE EXCITATIONS FROM THE ONE-CYCLE INTERACTION GREEN'S FUNCTION

The theoretical definition of SC is the existence of a nonvanishing order parameter χ [the thermal average of Eq. (4) in Paper I], while experimentally SC are usually characterized by the properties of their excitation spectrum, namely, the single-particle gap at the Fermi level [31]. This can be rather directly extracted from the solution to the Eliashberg equations on the imaginary axis since $\Delta^{\mathrm{E}}_{n=0}(J)$ is closely related to this excitation gap itself [23] and we use it in Fig. 5 for the J-T diagram.

The SC KS system of SpinSCDFT is designed to reproduce the densities of the interacting system, not the quasiparticle spectrum. On the other hand, for a normal metal the KS particles are often in good agreement with experiment so that the resulting KS excitation spectrum is used as an approximation to the interacting quasiparticle spectrum. With the potential $\Delta_s^s(\mathfrak{e})$ of Fig. 12 it turns out in SCDFT, also for the zero-field case [24], this is not always the case since, e.g., for $T \to 0$ the SC KS system is not gapped.

To predict a proper excitation spectrum without having to solve the many-body problem self-consistently we introduce the G_0W_0 approximation in the context of SC. This means to solve the Dyson equation once while replacing the interacting GF with the SC KS GF in the self-energy. Here, we use the same approximations for the self-energy made to arrive at the functional in I which means we use $\bar{\Sigma}^{\mathrm{KS}} = \bar{\Sigma}[\bar{G}^{\mathrm{KS}}]$ instead of the true self-energy $\bar{\Sigma}[\bar{G}]$.

In this section, we work in the isotropic formulation but note that the approach is easily generalized to the anisotropic case. We use the notation $\mathfrak{e} = \varepsilon, J, b$ and the isotropic Dyson equation

$$\bar{G}_n(\mathfrak{e}) = \left(\left[\bar{G}_n^{\mathrm{KS}}(\mathfrak{e})\right]^{-1} + \bar{\Sigma}_n^{\mathrm{KS}}(\mathfrak{e})\right)^{-1}, \tag{A1}$$

that follows from the assumption that the couplings depend on k via the center of energy $\frac{\varepsilon_{k\uparrow}-\varepsilon_{-k,\downarrow}}{2} \to \varepsilon$ and the splitting $\frac{\varepsilon_{k\uparrow}-\varepsilon_{-k,\downarrow}}{2} \to J$ and the isotropic bands b (that is a set of quantum numbers $\{k\}$). We introduce the notation $\bar{G}^{\alpha,\alpha'}_{n\sigma}(\mathfrak{e}) = \hat{I}_{k\sigma}(\mathfrak{e})\bar{G}^{\alpha,\alpha'}_{k\sigma,\pm k\pm\sigma}(\omega_n)$. The averaging procedure $\hat{I}_{k\sigma}(\mathfrak{e})$ on equal splitting and equal center-of-energy surfaces is defined in Eq. (131) of Paper I. We refer to the nonvanishing matrix elements with a spin label that refers to the first index of $\bar{G}^{\alpha,\alpha'}_{k\sigma,\pm k\pm\sigma}(\omega_n)$ and similarly for the self-energy.

1. Imaginary-axis formulation

The inversion of the Dyson equation (A1) to compute the GF explicitly is very analogous to the derivation of the Eliashberg equations in Paper I, Sec. IV A 1. We compute $\bar{G}_n(\mathfrak{e})$ via Eq. (A1) and the nonvanishing components are found to be [suppressing the arguments of $\mathfrak{F}_{n\sigma}(\mathfrak{e}), \Sigma_n^{\omega}(\mathfrak{e}), \Sigma_n^{J}(\mathfrak{e}), A_n^{\omega z}(\mathfrak{e}), \Sigma_n^{\mathrm{Re}\Delta}(\mathfrak{e}), \Sigma_n^{\mathrm{Im}\Delta}(\mathfrak{e})$, and $\Sigma_n^{t\pm}(\mathfrak{e})$]:

$$\bar{G}^{1,1}_{n\sigma} = \frac{1}{2\mathfrak{F}_{n\sigma}} \sum_{\alpha} \frac{\mathfrak{F}_{n\sigma} + \alpha\left[\varepsilon + \Sigma_n^{\varepsilon} + \mathrm{sign}(\sigma) A_n^{\omega z}\right]}{i\omega_n - \Sigma_n^{\omega} - \mathrm{sign}(\sigma)\left(J + \Sigma_n^{J}\right) - \alpha\mathfrak{F}_{n\sigma}}, \tag{A2}$$

$$\bar{G}^{-1,-1}_{n\sigma} = \frac{1}{2\mathfrak{F}_{n-\sigma}} \sum_{\alpha} \frac{\mathfrak{F}_{n-\sigma} + \alpha\left[\varepsilon + \Sigma_n^{\varepsilon} - \mathrm{sign}(\sigma) A_n^{\omega z}\right]}{i\omega_n - \Sigma_n^{\omega} + \mathrm{sign}(\sigma)\left(J + \Sigma_n^{J}\right) + \alpha\mathfrak{F}_{n-\sigma}}, \tag{A3}$$

$$\bar{G}^{1,-1}_{n\sigma} = \frac{\mathrm{sign}(\sigma)}{2\mathfrak{F}_{n\sigma}} \sum_{\alpha} \frac{\alpha\left(\Sigma_n^{\mathrm{Re}\Delta} + i\Sigma_n^{\mathrm{Im}\Delta} + \mathrm{sign}(\sigma)(\Sigma_n^{t-} + \Sigma_n^{t+})\right)}{i\omega_n - \Sigma_n^{\omega} - \mathrm{sign}(\sigma)\left(J + \Sigma_n^{J}\right) - \alpha\mathfrak{F}_{n\sigma}}, \tag{A4}$$

$$\bar{G}^{-1,1}_{n\sigma} = \frac{\mathrm{sign}(\sigma)}{2\mathfrak{F}_{n-\sigma}} \sum_{\alpha} \frac{\alpha\left(\Sigma^{\mathrm{Re}\Delta}_n - \mathrm{i}\Sigma^{\mathrm{Im}\Delta}_n + \mathrm{sign}(\sigma)(\Sigma^{\prime -}_n - \Sigma^{\prime +}_n)\right)}{i\omega_n - \Sigma^{\omega}_n + \mathrm{sign}(\sigma)\left(J + \Sigma^{J}_n\right) + \alpha\mathfrak{F}_{n-\sigma}} \tag{A5}$$

with

$$\begin{aligned}\mathfrak{F}_{n\sigma}(\mathfrak{e}) = \Big(\Big[\varepsilon + \Sigma^{\varepsilon}_n + \mathrm{sign}(\sigma)A^{\omega z}_n\Big]^2 \\ +\left[\Sigma^{\mathrm{Re}\Delta}_n + i\,\Sigma^{\mathrm{Im}\Delta}_n + \mathrm{sign}(\sigma)(\Sigma^{\prime +}_n + \Sigma^{\prime -}_n)\right] \\ \times\left[\Sigma^{\mathrm{Re}\Delta}_n - i\,\Sigma^{\mathrm{Im}\Delta}_n + \mathrm{sign}(\sigma)(\Sigma^{\prime +}_n - \Sigma^{\prime -}_n)\right]\Big)^{\frac{1}{2}},\end{aligned} \tag{A6}$$

where the self-energy parts are constructed similar to the Eliashberg theory with the result

$$\Sigma^{\omega}_n = \frac{1}{4}\sum_{\sigma}\left(\bar{\Sigma}^{\mathrm{KS}1,1}_{\sigma n} + \bar{\Sigma}^{\mathrm{KS}-1,-1}_{\sigma n}\right), \tag{A7}$$

$$A^{\omega z}_n = \frac{1}{4}\sum_{\sigma}\mathrm{sign}(\sigma)\left(\bar{\Sigma}^{\mathrm{KS}1,1}_{\sigma n} + \bar{\Sigma}^{\mathrm{KS}-1,-1}_{\sigma n}\right), \tag{A8}$$

$$\Sigma^{\varepsilon}_n = \frac{1}{4}\sum_{\sigma}\left(\bar{\Sigma}^{\mathrm{KS}1,1}_{\sigma n} - \bar{\Sigma}^{\mathrm{KS}-1,-1}_{\sigma n}\right), \tag{A9}$$

$$\Sigma^{J}_n = \frac{1}{4}\sum_{\sigma}\mathrm{sign}(\sigma)\left(\bar{\Sigma}^{\mathrm{KS}1,1}_{\sigma n} - \bar{\Sigma}^{\mathrm{KS}-1,-1}_{\sigma n}\right), \tag{A10}$$

$$\Sigma^{\prime +}_n = \frac{1}{4}\sum_{\sigma}\left(\bar{\Sigma}^{\mathrm{KS}1,-1}_{\sigma n} + \bar{\Sigma}^{\mathrm{KS}-1,1}_{\sigma n}\right), \tag{A11}$$

$$\Sigma^{\prime -}_n = \frac{1}{4}\sum_{\sigma}\left(\bar{\Sigma}^{\mathrm{KS}1,-1}_{\sigma n} - \bar{\Sigma}^{\mathrm{KS}-1,1}_{\sigma n}\right), \tag{A12}$$

$$\Sigma^{\mathrm{Im}\Delta}_n = \frac{-\mathrm{i}}{4}\sum_{\sigma}\mathrm{sign}(\sigma)\left(\bar{\Sigma}^{\mathrm{KS}1,-1}_{\sigma n} + \bar{\Sigma}^{\mathrm{KS}-1,1}_{\sigma n}\right), \tag{A13}$$

$$\Sigma^{\mathrm{Re}\Delta}_n = \frac{1}{4}\sum_{\sigma}\mathrm{sign}(\sigma)\left(\bar{\Sigma}^{\mathrm{KS}1,-1}_{\sigma n} - \bar{\Sigma}^{\mathrm{KS}-1,1}_{\sigma n}\right). \tag{A14}$$

Note, however, that $\bar{\Sigma}^{\mathrm{KS}1,-1}_{\sigma n}$ contains a triplet contribution that is generated by the coupling imbalance of the spin channels. The isotropic variants of the Eqs. (67) to (70) of paper I are given by

$$\begin{aligned}\Sigma^{\mathrm{KS}1,1}_{\mathrm{ph}\,\sigma n} = \int d\Omega \int d\mathfrak{e}'\,\alpha^2 F^{\mathrm{D}}_{\sigma}(\mathfrak{e},\mathfrak{e}',\Omega) \\ \times\sum_{\alpha}\frac{\alpha\varepsilon' + F'}{2F'}M_{\mathrm{ph}}\left(\Omega, E^{\alpha\prime}_{\sigma},\omega_n\right),\end{aligned} \tag{A15}$$

$$\begin{aligned}\Sigma^{\mathrm{KS}-1,-1}_{\mathrm{ph}\,\sigma n} = \int d\Omega \int d\mathfrak{e}'\,\alpha^2 F^{\mathrm{D}}_{\sigma}(\mathfrak{e},\mathfrak{e}',\Omega) \\ \times\sum_{\alpha}\frac{\alpha\varepsilon' + F'}{2F'}M_{\mathrm{ph}}\left(\Omega, -E^{\alpha\prime}_{\sigma},\omega_n\right),\end{aligned} \tag{A16}$$

$$\begin{aligned}\Sigma^{\mathrm{KS}1,-1}_{\mathrm{ph}\,\sigma n} = -\mathrm{sign}(\sigma)\int d\Omega \int d\mathfrak{e}'\,\alpha^2 F(\mathfrak{e},\mathfrak{e}',\Omega) \\ \times\sum_{\alpha}\frac{\alpha\Delta^{s\prime}_{\mathrm{s}}}{2F'}M_{\mathrm{ph}}\left(\Omega, E^{\alpha\prime}_{\sigma},\omega_n\right),\end{aligned} \tag{A17}$$

$$\begin{aligned}\Sigma^{\mathrm{KS}-1,1}_{\mathrm{ph}\,\sigma n} = -\mathrm{sign}(\sigma)\int d\Omega \int d\mathfrak{e}'\,\alpha^2 F(\mathfrak{e},\mathfrak{e}',\Omega) \\ \times\sum_{\alpha}\frac{\alpha\Delta^{s\prime *}_{\mathrm{s}}}{2F'}M_{\mathrm{ph}}\left(\Omega, -E^{\alpha\prime}_{\sigma},\omega_n\right)\end{aligned} \tag{A18}$$

with $\Delta^{s\prime}_{\mathrm{s}}$ shorthand for $\Delta^{s}_{\mathrm{s}}(\mathfrak{e}')$, the averaged $\Delta^{s}_{\mathrm{s}k}$ and $F' = \sqrt{\varepsilon'^2 + \Delta^{s\prime 2}_{\mathrm{s}}}$. Furthermore, $E^{\alpha\prime}_{\sigma} = \mathrm{sign}(\sigma)J + \mathrm{sign}(\alpha)F'$ and similarly Eqs. (76) and (77) of Paper I become

$$\Sigma^{\mathrm{KS}1,-1}_{\mathrm{C}\,\sigma n} = -\mathrm{sign}(\sigma)\sum_{\alpha}\int d\mathfrak{e}'\frac{\alpha\Delta^{s\prime}_{s}}{2F'}C^{\mathrm{stat}}(\mathfrak{e},\mathfrak{e}')f_{\beta}\left(E^{\alpha\prime}_{\sigma}\right), \tag{A19}$$

$$\Sigma^{\mathrm{KS}-1,1}_{\mathrm{C}\,\sigma n} = -\mathrm{sign}(\sigma)\sum_{\alpha}\int d\mathfrak{e}'\frac{\alpha\Delta^{s\prime *}_{s}}{2F'}C^{\mathrm{stat}}(\mathfrak{e},\mathfrak{e}')f_{\beta}\left(-E^{\alpha\prime}_{\sigma}\right). \tag{A20}$$

With these equations we can compute the G_0W_0 GF from the results of a converged SpinSCDFT calculation.

2. Real-axis formulation

To obtain the (L)DOS from the temperature GF we substitute

$$i\omega_n \to \omega + i\eta, \tag{A21}$$

where η is a real positive infinitesimal [32]. The expressions (A2)–(A5) remain essentially unchanged on the real axis, except that we have to insert the self-energy (SE) parts (A7)–(A14) on the real axis and write $i\eta + \omega$ instead of the Matsubara frequency. Here, we have two options: first we may compute the SE parts on the imaginary axis and use a numerical analytic continuation to the real axis, or we can compute analytic formulas for the real axis and use them. We choose the latter because this avoids the sometimes unstable analytical continuation.

We will see that the SE parts, e.g., $\Sigma^{\mathrm{Re}\Delta}_n(\mathfrak{e})$, on the real axis have to be computed via independent calculations of imaginary and real parts. The dependence on the Matsubara index of the SE is only via the function M_{ph} of Eq. (74) of Paper I, i.e., the results of the first Matsubara summation in the SE. Thus, on the real axis

$$\begin{aligned}M_{\mathrm{ph}}(\Omega,E,\omega) = \hat{\mathrm{P}}\frac{n_{\beta}(\Omega) + f_{\beta}(E)}{\Omega - E + \omega} - \hat{\mathrm{P}}\frac{n_{\beta}(\Omega) + f_{\beta}(-E)}{\Omega + E - \omega} \\ - i\pi([n_{\beta}(\Omega) + f_{\beta}(E)]\delta(\Omega - E + \omega) \\ + [n_{\beta}(\Omega) + f_{\beta}(-E)]\delta(\Omega + E - \omega)).\end{aligned} \tag{A22}$$

Here, $\hat{\mathrm{P}}$ is the principal-value operator. Because of the very different nature of the imaginary and real parts of the SE we compute both parts independently. Then, we obtain

$$\begin{aligned}\mathrm{Im}\Sigma^{\omega}(\mathfrak{e},\omega) = -\pi\int d\mathfrak{e}'\sum_{\mu\alpha}\frac{\alpha\varepsilon' + F'}{8F'}\Big(\left[n_{\beta}\left(E^{\alpha\prime}_{\mu} - \omega\right) + f_{\beta}\left(E^{\alpha\prime}_{\mu}\right)\right]\left[\alpha^2 F^{\mathrm{D}}_{\mu}\left(\mathfrak{e},\mathfrak{e}',E^{\alpha\prime}_{\mu} - \omega\right) - \alpha^2 F^{\mathrm{D}}_{\mu}\left(\mathfrak{e},\mathfrak{e}',\omega - E^{\alpha\prime}_{\mu}\right)\right] \\ + \left[n_{\beta}\left(E^{\alpha\prime}_{\mu} + \omega\right) + f_{\beta}\left(E^{\alpha\prime}_{\mu}\right)\right]\left[\alpha^2 F^{\mathrm{D}}_{\mu}\left(\mathfrak{e},\mathfrak{e}',E^{\alpha\prime}_{\mu} + \omega\right) - \alpha^2 F^{\mathrm{D}}_{\mu}\left(\mathfrak{e},\mathfrak{e}', -E^{\alpha\prime}_{\mu} - \omega\right)\right]\Big),\end{aligned} \tag{A23}$$

$$\mathrm{Re}\Sigma^{\omega}(\mathfrak{e},\omega) = \int d\Omega \int d\mathfrak{e}' \sum_{\mu\alpha} \frac{\alpha\varepsilon' + F'}{8F'} \alpha^2 F^{\mathrm{D}}_{\mu}(\mathfrak{e},\mathfrak{e}',\Omega) \Big(\hat{\mathrm{P}} \frac{n_\beta(\Omega) + f_\beta\big(E^{\alpha'}_{\mu}\big)}{\Omega - E^{\alpha'}_{\mu} + \omega} - \hat{\mathrm{P}} \frac{n_\beta(\Omega) + f_\beta\big(E^{\alpha'}_{\mu}\big)}{\Omega - E^{\alpha'}_{\mu} - \omega} - \hat{\mathrm{P}} \frac{n_\beta(\Omega) + f_\beta\big(-E^{\alpha'}_{\mu}\big)}{\Omega + E^{\alpha'}_{\mu} - \omega} + \hat{\mathrm{P}} \frac{n_\beta(\Omega) + f_\beta\big(-E^{\alpha'}_{\mu}\big)}{\Omega + E^{\alpha'}_{\mu} + \omega} \Big), \tag{A24}$$

$$\mathrm{Im}\Sigma^{\varepsilon}(\mathfrak{e},\omega) = -\pi \int d\mathfrak{e}' \sum_{\mu\alpha} \frac{\alpha\varepsilon' + F'}{8F'} \big(\big[n_\beta\big(E^{\alpha'}_{\mu} - \omega\big) + f_\beta\big(E^{\alpha'}_{\mu}\big) \big] \big[\alpha^2 F^{\mathrm{D}}_{\mu}\big(\mathfrak{e},\mathfrak{e}', E^{\alpha'}_{\mu} - \omega\big) - \alpha^2 F^{\mathrm{D}}_{\mu}\big(\mathfrak{e},\mathfrak{e}', \omega - E^{\alpha'}_{\mu}\big) \big] - \big[n_\beta\big(E^{\alpha'}_{\mu} + \omega\big) + f_\beta\big(E^{\alpha'}_{\mu}\big) \big] \big[\alpha^2 F^{\mathrm{D}}_{\mu}\big(\mathfrak{e},\mathfrak{e}', E^{\alpha'}_{\mu} + \omega\big) - \alpha^2 F^{\mathrm{D}}_{\mu}\big(\mathfrak{e},\mathfrak{e}', -E^{\alpha'}_{\mu} - \omega\big) \big] \big), \tag{A25}$$

$$\mathrm{Re}\Sigma^{\varepsilon}(\mathfrak{e},\omega) = \int d\Omega \int d\mathfrak{e}' \sum_{\mu\alpha} \frac{\alpha\varepsilon' + F'}{8F'} \alpha^2 F^{\mathrm{D}}_{\mu}(\mathfrak{e},\mathfrak{e}',\Omega) \Big(\hat{\mathrm{P}} \frac{n_\beta(\Omega) + f_\beta(E^{\alpha'}_{\mu})}{\Omega - E^{\alpha'}_{\mu} + \omega} + \hat{\mathrm{P}} \frac{n_\beta(\Omega) + f_\beta(E^{\alpha'}_{\mu})}{\Omega - E^{\alpha'}_{\mu} - \omega} - \hat{\mathrm{P}} \frac{n_\beta(\Omega) + f_\beta(-E^{\alpha'}_{\mu})}{\Omega + E^{\alpha'}_{\mu} - \omega} - \hat{\mathrm{P}} \frac{n_\beta(\Omega) + f_\beta(-E^{\alpha'}_{\mu})}{\Omega + E^{\alpha'}_{\mu} + \omega} \Big) \tag{A26}$$

and very similar for $A^{\omega z}(\mathfrak{e}\omega)$ that only differs from Σ^{ω} by putting a $\mathrm{sign}(\mu)$ into the spin sums. We also obtain $\Sigma^{J}(\mathfrak{e}\omega)$ from the relation for $\Sigma^{\varepsilon}(\mathfrak{e},\omega)$ in the same way, i.e., we put a $\mathrm{sign}(\mu)$ into the spin sum. The above equation again points out the problem in the ε' integral if the energy dependence of $\alpha^2 F^{\mathrm{D}}_{\mu}(\mathfrak{e},\mathfrak{e}',\Omega)$ is neglected. Here, $E^{\alpha'}_{\mu} \to \alpha|\varepsilon'|$ for large $|\varepsilon'|$ so there are parts in the integral that behave as $\frac{1}{\varepsilon'}$ leading to logarithmic divergence. Thus, we see explicitly that we cannot compute the energy renormalization without considering the influence of the interaction on the full energy spectrum and quasiparticle occupations as was already discussed in I and Ref. [11].

We define the integrand

$$\mathrm{Im}\mathcal{B}_{\pm}(\mathfrak{e},\mathfrak{e}',\omega) = \pi \sum_{\mu\alpha} \mathrm{sign}(\mu)^{\frac{1\pm1}{2}} \frac{\mathrm{sign}(\alpha)}{2F'} \big[n_\beta\big(E^{\alpha'}_{\mu} - \omega\big) + f_\beta\big(E^{\alpha'}_{\mu}\big) \big] \big[\alpha^2 F^{\mathrm{D}}_{\mu}\big(\mathfrak{e},\mathfrak{e}', E^{\alpha'}_{\mu} - \omega\big) - \alpha^2 F^{\mathrm{D}}_{\mu}\big(\mathfrak{e},\mathfrak{e}', \omega - E^{\alpha'}_{\mu}\big) \big], \tag{A27}$$

$$\mathrm{Re}\mathcal{B}_{\pm}(\mathfrak{e},\mathfrak{e}',\omega) = -\sum_{\mu\alpha} \mathrm{sign}(\mu)^{\frac{1\pm1}{2}} \frac{\mathrm{sign}(\alpha)}{4F'} \Big[\int d\Omega\, \alpha^2 F^{\mathrm{D}}_{\mu}(\mathfrak{e},\mathfrak{e}',\Omega) \Big(\hat{\mathrm{P}} \frac{n_\beta(\Omega) + f_\beta(E^{+'}_{\mu})}{\Omega - E^{+'}_{\mu} + \omega} - \hat{\mathrm{P}} \frac{n_\beta(\Omega) + f_\beta(-E^{\alpha'}_{\mu})}{\Omega + E^{\alpha'}_{\mu} - \omega} \Big) + f_\beta(E^{\alpha'}_{\mu}) C^{\mathrm{stat}}(\mathfrak{e},\mathfrak{e}') \Big] \tag{A28}$$

and further introducing

$$B^{s}_{n}(\mathfrak{e}) \equiv \Sigma^{\mathrm{Re}\Delta}_{n}(\mathfrak{e}) + \mathrm{i}\Sigma^{\mathrm{Im}\Delta}_{n}(\mathfrak{e}), \tag{A29}$$

$$B^{s\star}_{n}(\mathfrak{e}) \equiv \Sigma^{\mathrm{Re}\Delta}_{n}(\mathfrak{e}) - \mathrm{i}\Sigma^{\mathrm{Im}\Delta}_{n}(\mathfrak{e}), \tag{A30}$$

$$B^{t}_{n}(\mathfrak{e}) \equiv \Sigma^{t+}_{n}(\mathfrak{e}) + \Sigma^{t-}_{n}(\mathfrak{e}), \tag{A31}$$

$$B^{t\star}_{n}(\mathfrak{e}) \equiv \Sigma^{t+}_{n}(\mathfrak{e}) - \Sigma^{t-}_{n}(\mathfrak{e}), \tag{A32}$$

we obtain the following equations on the real axis:

$$B^{s}(\mathfrak{e},\omega) = \int d\mathfrak{e}' \Delta^{s}_{s}{}' \mathcal{B}_{-}(\mathfrak{e},\mathfrak{e}',\omega), \tag{A33}$$

$$B^{s\star}(\mathfrak{e},\omega) = \int d\mathfrak{e}' \Delta^{s'*}_{s} \mathcal{B}_{-}(\mathfrak{e},\mathfrak{e}',\omega), \tag{A34}$$

$$B^{t}(\mathfrak{e},\omega) = \int d\mathfrak{e}' \Delta^{s}_{s}{}' \mathcal{B}_{+}(\mathfrak{e},\mathfrak{e}',\omega), \tag{A35}$$

$$B^{t\star}(\mathfrak{e},\omega) = \int d\mathfrak{e}' \Delta^{s'*}_{s} \mathcal{B}_{+}(\mathfrak{e},\mathfrak{e}',\omega), \tag{A36}$$

and, thus, Eq. (A6) becomes on the real axis (omitting the arguments $\mathfrak{e},\omega$)

$$\mathfrak{F}_{\sigma} = ([\varepsilon + \Sigma^{\varepsilon} + \mathrm{sign}(\sigma) A^{\omega z}]^2 + [B^{s} + \mathrm{sign}(\sigma) B^{t}][B^{s\star} + \mathrm{sign}(\sigma) B^{t\star}])^{\frac{1}{2}}. \tag{A37}$$

Now, we can finally obtain the retarded GF with the equations from Eqs. (A2)–(A5) together with Eq. (A6) for $\mathfrak{F}_{n\sigma}(\mathfrak{e})$ in terms of B and the corresponding SE parts constructed from real and imaginary parts close to the real axis. Then, we can evaluate the DOS according to

$$\rho_{\sigma\alpha}(\omega) = -2 \int d\mathfrak{e}\, \mathrm{Im}\Big(\lim_{\eta\to 0} \lim_{i\omega_n \to \omega + \mathrm{i}\eta} \bar{G}^{\alpha,\alpha}_{n\sigma}(\mathfrak{e}) \Big) \varrho(\mathfrak{e}). \tag{A38}$$

We obtain the local DOS $\rho_{\sigma\alpha}(\mathbf{r},\omega)$ simply by replacing $\varrho(\mathfrak{e})$ with the local double DOS $\varrho_{\sigma}(\mathfrak{e},\boldsymbol{r}) = \hat{I}_{k\sigma}(\mathfrak{e})|\varphi_k(\boldsymbol{r}\sigma)|^2$.

[1] S. S. Saxena, P. Agarwal, K. Ahilan, F. M. Grosche, R. K. W. Haselwimmer, M. J. Steiner, E. Pugh, I. R. Walker, S. R. Julian, P. Monthoux, G. G. Lonzarich, A. Huxley, I. Sheikin, D. Braithwaite, and J. Flouquet, Nature (London) **406**, 587 (2000).
[2] A. I. Larkin and Yu. N. Ovchinnikov, ZhETF **47**, 1136 (1964) [Sov. Phys. JETP **20**, 762 (1965)].
[3] P. Fulde and R. A. Ferrell, Phys. Rev. **135**, A550 (1964).
[4] L. R. Tagirov, Phys. Rev. Lett. **83**, 2058 (1999).
[5] A. I. Buzdin, A. V. Vedyayev, and N. V. Ryzhanova, Europhys. Lett. **48**, 686 (1999).
[6] J. Y. Gu, C.-Y. You, J. S. Jiang, J. Pearson, Y. B. Bazaliy, and S. D. Bader, Phys. Rev. Lett. **89**, 267001 (2002).
[7] A. I. Buzdin, Rev. Mod. Phys. **77**, 935 (2005).
[8] A. Linscheid, A. Sanna, F. Essenberger, and E. K. U. Gross, Phys. Rev. B **92**, 024505 (2015).
[9] L. J. Sham and M. Schlüter, Phys. Rev. Lett. **51**, 1888 (1983).
[10] M. Marques, Density Functional Theory for Superconductors: Exchange and Correlation Potentials for Inhomogeneous Systems, Ph.D. thesis, University of Würzburg, 2000.
[11] M. Lüders, M. A. L. Marques, N. N. Lathiotakis, A. Floris, G. Profeta, L. Fast, A. Continenza, S. Massidda, and E. K. U. Gross, Phys. Rev. B **72**, 024545 (2005).
[12] M. A. L. Marques, M. Lüders, N. N. Lathiotakis, G. Profeta, A. Floris, L. Fast, A. Continenza, E. K. U. Gross, and S. Massidda, Phys. Rev. B **72**, 024546 (2005).
[13] S. Vonsovsky, Y. Izyumov, E. Kurmaev, E. Brandt, and A. Zavarnitsyn, *Superconductivity of Transition Metals: Their Alloys and Compounds*, Springer Series in Solid-State Sciences Series (Springer, London, 1982).
[14] G. Sarma, J. Phys. Chem. Solids **24**, 1029 (1963).
[15] M. S. Hybertsen and S. G. Louie, Phys. Rev. Lett. **55**, 1418 (1985).
[16] P. B. Allen and B. Mitrović, in *Theory of Superconducting* T_c, edited by F. S. Henry Ehrenreich and D. Turnbull, Solid State Physics, Vol. 37 (Academic, New York, 1983), pp. 1–92.
[17] K.-P. Bohnen, R. Heid, and B. Renker, Phys. Rev. Lett. **86**, 5771 (2001).
[18] S. Massidda, F. Bernardini, C. Bersier, A. Continenza, P. Cudazzo, A. Floris, H. Glawe, M. Monni, S. Pittalis, G. Profeta, A. Sanna, S. Sharma, and E. K. U. Gross, Supercond. Sci. Technol. **22**, 034006 (2009).
[19] J. Bardeen, L. N. Cooper, and J. R. Schrieffer, Phys. Rev. **108**, 1175 (1957).
[20] B. S. Chandrasekhar, Appl. Phys. Lett. **1**, 7 (1962).
[21] A. M. Clogston, Phys. Rev. Lett. **9**, 266 (1962).
[22] B. J. Powell, J. F. Annett, and B. L. Györffy, J. Phys. A: Math. Gen. **36**, 9289 (2003).
[23] J. P. Carbotte, Rev. Mod. Phys. **62**, 1027 (1990).
[24] A. Sanna and E. K. U. Gross (unpublished).
[25] D. J. Scalapino, J. R. Schrieffer, and J. W. Wilkins, Phys. Rev. **148**, 263 (1966).
[26] P. Morel and P. W. Anderson, Phys. Rev. **125**, 1263 (1962).
[27] H. Fröhlich, Proc. R. Soc. Lond., Ser. A **215**, 291 (1952).
[28] A. Floris, G. Profeta, N. N. Lathiotakis, M. Lüders, M. A. L. Marques, C. Franchini, E. K. U. Gross, A. Continenza, and S. Massidda, Phys. Rev. Lett. **94**, 037004 (2005).
[29] J. M. An and W. E. Pickett, Phys. Rev. Lett. **86**, 4366 (2001).
[30] W. L. McMillan, Phys. Rev. **167**, 331 (1968).
[31] A. Damascelli and Z.-X. Shen, Rev. Mod. Phys. **75**, 473 (2003).
[32] A. Fetter and J. Walecka, *Quantum Theory of Many-particle Systems*, Dover Books on Physics Series (Dover, New York, 1971).